

# Vanishing Depth: A Depth Adapter with Positional Depth Encoding for Generalized Image Encoders

Paul Koch<sup>1\*</sup> Jörg Krüger<sup>1,2</sup> Oliver Heimann<sup>1</sup> Ankit Chowdhury<sup>1</sup>

## Abstract

Generalized metric depth understanding is critical for precise vision-guided robotics, which current state-of-the-art (SOTA) vision-encoders do not support. To address this, we propose Vanishing Depth, a self-supervised training approach that extends pretrained RGB encoders to incorporate and align metric depth into their feature embeddings. Based on our novel positional depth encoding, we enable stable depth density and depth distribution invariant feature extraction. We achieve performance improvements and SOTA results across a spectrum of relevant RGBD downstream tasks - without the necessity of finetuning the encoder. Most notably, we achieve 56.05 mIoU on SUN-RGBD segmentation, 88.3 RMSE on Void’s depth completion, and 83.8 Top 1 accuracy on NYUv2 scene classification. In 6D-object pose estimation, we outperform our predecessors of DinoV2, EVA-02, and Omnivore and achieve SOTA results for non-finetuned encoders in several related RGBD downstream tasks.

**Code:** <https://github.com/KochPJ/vanishing-depth>

## 1. Introduction

Self-supervised learning (SSL) has emerged as a crucial innovation in the development of generalized models, also called foundation models (Bommasani et al., 2021). These models use task-agnostic SSL representation learning to extract generalized features that can be used for downstream tasks without the need for further finetuning (Brown et al., 2020; Oquab et al., 2023). In fact, small-sized supervised finetuning might even corrupt and destroy generalized feature extraction (Mukhoti et al., 2024). This independence from task specific finetuning distinguishes foundation models from the traditional transfer learning. Foundation models yield a faster and more efficient generalized adapta-

tion (Brown et al., 2020). Moreover, they allow one to append multiple heads for a multi-task system with a shared feature extraction. This in turn further increases efficiency, as the encoder is often by far the biggest module in AI-based computer vision and enables fast modular updates.

We observe a general push towards foundation models that are capable of process multiple input modalities. Within computer vision, Omnivore (Girdhar et al., 2022) and OmniVec (Srivastava & Sharma, 2023) use multi-modal pre-training to create generalized multi modal capable vision encoders with promising properties. LLaVa (Liu et al., 2023), Clip (Radford et al., 2021) and EVA (Fang et al., 2022; 2024) employ text-image encoders that yield SOTA results. However, most related research on generalized vision encoders focuses preliminary on RGB information (He et al., 2021; Zhou et al., 2021; Oquab et al., 2023; Fang et al., 2024). Here, we observe a lack of vision encoders with metric depth understanding in the literature, which seem especially crucial for downstream tasks which require absolute 3D position information, such as robotics.

We propose a novel SSL training pipeline, termed Vanishing Depth (VD), that extends generalized pretrained RGB encoders, like DINOv2, to extract and incorporate depth features into their latent space. Through this approach, we demonstrate a generalized metric depth-aware RGBD encoder capable of addressing various RGBD downstream tasks without the need for additional finetuning. Furthermore, we introduce positional depth encoding (PDE), a novel depth encoding technique following the original positional encoding (Vaswani et al., 2017). In our experiments, this technique proves to be precise and exhibits stable scalability, when applied to novel depth distributions and densities, resulting in SOTA results of 56.05 mIoU on SUN-RGBD (Song et al., 2015) segmentation and 88.3 RMSE on Void’s (Wong et al., 2020) depth completion.

## 2. Related Work

SSL-pretrained depth encoders have demonstrated their value in solving RGBD downstream tasks (e.g. (Yin et al., 2023)). However, these encoders are often tailored for specific tasks and lack the generalizability offered by,

\*Primary contribution <sup>1</sup>Fraunhofer IPK, Pascalstraße 8-9, 10587 Berlin, Germany <sup>2</sup>Technische Universität Berlin, Pascalstraße 8-9, 10587 Berlin, Germany. Correspondence to: Paul Koch <paul.koch@ipk.fraunhofer.de>.

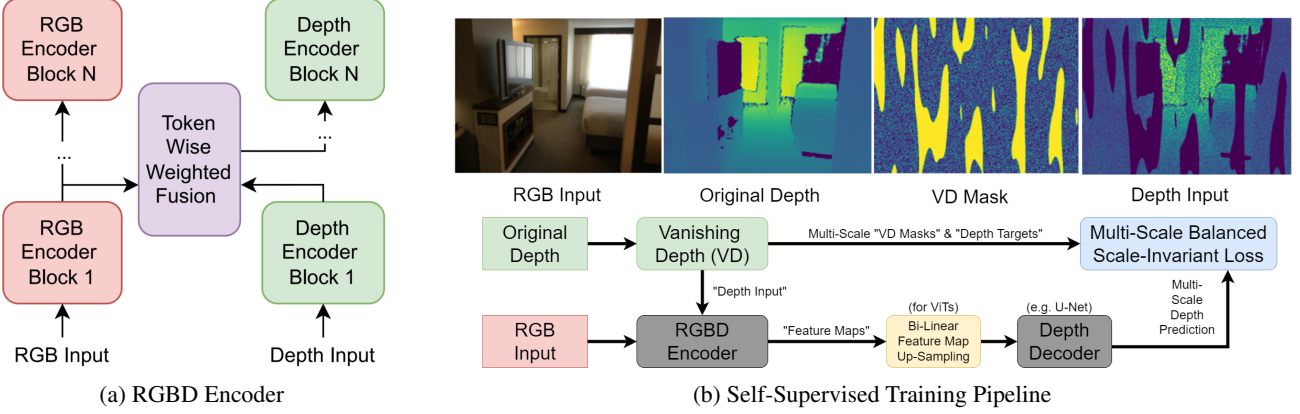


**Figure 1. Vanishing Depth:** We use perlin and random noise to remove depth information from the original depth image. The remaining depth information is then passed through an RGBD encoder and FPN decoder network (Lin et al., 2016). Using multi-scale noise masks, we calculate and evenly combine the scale-invariant loss for reconstructing the input depth and predicting missing depth inputs at multiple downstream stages of the network. After training, we remove the decoder, resulting in a pretrained RGBD encoder.

e.g. DINOv2 (Quab et al., 2023). However, SOTA methods for RGBD segmentation often leave the depth encoder randomly initialized, relying solely on supervised training (Wang et al., 2022b; Zhang et al., 2023; Seichter et al., 2023; Jia et al., 2024). Other related work employs SSL methods such as inpainting (Ning et al., 2023), and combinations of monocular depth estimation with recolorizing (Zhao et al., 2021). Other explore new depth SSL options such as modality-fusion (Valada et al., 2018), segmentation label generation (Lahoud & Ghanem, 2020), and 3D-predictions (Li & Heizmann, 2022). However, these methods are often task specific and do not scale towards a broad application. Multi modal encoders such as Omnidore (Girdhar et al., 2022), Omnidore (Srivastava & Sharma, 2023), and OmniVec2 (Srivastava & Sharma, 2024) use token-based fusion and align the sample wise feature extraction within the latent space. While Omnidore does this with supervised learning, OmniVec uses contrastive MiM (Hondu et al., 2025) to pretrain their encoders, while OmniVec2 uses a discriminative SSL approach (see, e.g. Dino (Caron et al., 2021)). However, these training methods do not explicitly guide their depth feature extraction to be precise or metric. They only align the context of the input modalities, and do not impose pressure on pixel-wise input unit precision. We demonstrate this inaccuracy for Omnidore in our depth completion and pose estimation experiments. In contrast to these aforementioned methods, the SSL MAE-like (He et al., 2021) RGB-guided depth completion (Jaritz et al., 2018; Gansbeke et al., 2019; Park et al., 2020; Hu et al., 2021; Yan et al., 2021; Nazir et al., 2022) uses the semantic RGB information to guide the prediction of missing depth values. This trains both semantic understanding and precise metric depth feature extraction. We follow this approach to align depth feature extraction with the latent space of pretrained RGB encoders for metric depth understanding.

### 3. Vanishing Depth (VD)

Our VD pretraining pipeline (see Fig. 1) is inspired by previous work in-painting (Pathak et al., 2016; Ning et al., 2023), monocular depth estimation (Eigen et al., 2014; Eigen & Fergus, 2014), and color-guided depth completion (Hu et al., 2021). We combine these into VD to create a generalized RGBD encoder which can be used for a wide range of unseen downstream tasks, without training an RGBD encoder from scratch or finetuning. It leverages existing pretrained RGB encoders to benefit from their generalized feature extraction. The extracted color features should be fused into depth embeddings at various states in the depth encoder latent space. This leaves the pretrained RGB encoder unscaved and allows the depth encoder to incorporate hierarchical RGB embeddings. In addition, the RGBD encoder should be able to handle various input distributions, densities, and related downstream tasks. Therefore, we introduce: A) positional depth encoding (PDE) for stable continuous real number embeddings; B) depth randomization to achieve depth distribution invariance; C) random depth completion to achieve depth density invariance; and D) a multi-scale balanced scale-invariant loss to balance the depth completion between reconstruction and prediction throughout the encoder stages.

#### 3.1. Positional Depth Encoding (PDE)

Depth images, unlike RGB images, pose challenges to the commonly used normalization-based encoding method due to their positive continuous real numbers. Depth signals can have infinite growth, resulting in large and precise input values, which can cause unstable training behavior and exploding gradients (Eigen et al., 2014). Moreover, using a large standard deviation to counter this issue pushes minor depth features down the decimal places, making them hardly dis-

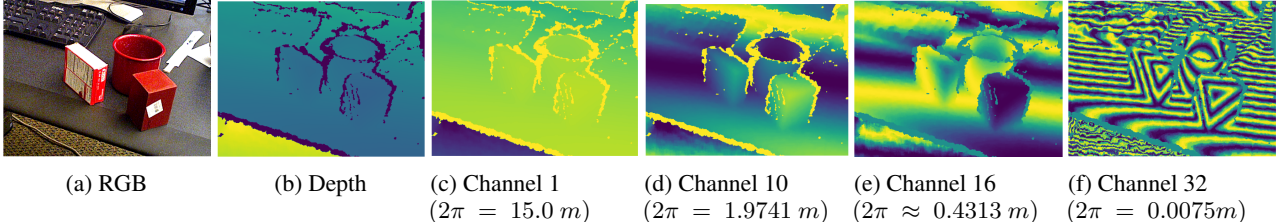


**Figure 2. Visualisation of Positional Depth Encoding (PDE):** Example of PDE with 32 channels (16 cosine and sine frequency pairs) and max depth  $max_d = 15\text{m}$ . The first frequency (c) captures large changes in depth image, while the final frequency (f) encodes minor depth changes.

tinguishable from noise, and complicates feature extraction. It is important to note that depth images often have missing values filled with zeros, which can significantly affect the input distribution when the number of zeros changes. Although other encoding methods such as HHA (Gupta et al., 2014) or disparity maps attempt to address these challenges, they sacrifice metric depth and for HHA require heavy pre-processing computations. To overcome these limitations we adopt positional encoding (Vaswani et al., 2017) and propose positional "Depth" encoding (PDE):

$$\begin{aligned} PDE(d_j, 2i) &= \sin(2\pi \times d_j / max_d / T^{2i/Ch.}) \\ PDE(d_j, 2i + 1) &= \cos(2\pi \times d_j / max_d / T^{2i/Ch.}) \end{aligned} \quad (1)$$

where  $i$  is the PDE channel and  $d_j$  is the a depth pixel of the depth map  $d \in D$ , and  $D$  is the input depth distribution.  $Ch.$  the number of desired depth channels in PDE.  $T < 1$  is the temperature that defines the frequency distribution and the smallest frequency (precision) of PDE.

$$max_d = \begin{cases} max(D), & \text{if using Global Max Depth} \\ max(d), & \text{otherwise} \end{cases} \quad (2)$$

normalizes the input depth. If not using a global max depth, the model needs to encode  $max_d$  to be able to decode the randomized depth (see Sec. 3.2). Otherwise, the model can learn the constant global max scalar during training. For ViTs (Dosovitskiy et al., 2020), we encode  $max_d = max(D)$  in a vector  $V$  and add it to the depth encoder's cls token. We vectorize  $max_d$  by encoding its integer and decimal values  $v$  by  $V_i = (v_i + 1)/10$ . We pad the vector with zeros to fit the size of the cls token and hold the separation index between integer and decimal values constant at 64. This enables the model to read any  $max_d$  with up to 64 integer and decimal places, keeps the integer and decimal positions constant, and marks the start, stop, and missing value indexes with zeros. PDE ensures stable input and feature extraction within the range of -1 and 1, regardless of the input distribution or absolute depth (see Fig. 2). However, PDE increases the computational cost linearly by a factor of  $ch.$  in the first convolution or fully-connected encoding layer, and limits the encoding precision

to the distribution ( $T$ ) and the number of encoding frequencies ( $Ch.$ ). In summery, PDE differs too classical PE in that it allows dynamic input normalization, which can be decoded with the correct key into metric depth. Moreover, we use  $T < 1$  so that it defines the smallest frequency, which is more intuitive for depth.

**Positional 3D Encoding (P3DE):** Our proposed PDE encoding and MS-decode enable point cloud processing as well. Using random generated camera intrinsics, we convert depth images into 3D points. We use only positive numbers, as we can deduce the XY sign from the pixel coordinates, effectively excluding the need to handle negative numbers in both the encoder and decoder. For depth encoding, we employ our normal PDE to encode the XYZ values individually and stack the channels.

### 3.2. Randomized Depth

**Distribution Invariance:** A key factor in our VD training pipeline is to randomly manipulate the depth images by rescaling and offsetting them. This prevents monocular depth estimation from the RGB encoder, as each target depth training sample can have numerous variations. Thus, the model has to combine semantic RGB with depth embeddings, which indicate the current distances. We employ random offset, random depth scalar, and rescaling of the depth image within specific minimum and maximum values drawn from jittered bins. The bins ensure that larger numbers are not overrepresented. This enables the depth encoder to handle any depth distribution.

**Density Invariance:** To train inpainting models, binary masks or similar markings are required to indicate the areas to be removed. Some approach this with masked grids (He et al., 2021; Ning et al., 2023; Bao et al., 2021; El-Nouby et al., 2021) or generate random noise with a threshold from a given distribution to obtain the binary mask. This can be applied to different scales of the input size, which are then up-sampled to control the size of the removed areas. Another approach is to use perlin noise, which provides random noise with in size varying organic rounded shapes. We use both approaches to: A) mimic sparse lidar depth

**Table 1. VD & PDE Ablation:** We compare PDE vs. related work on depth encoding methods such as; Omnivore’s normalize disparity maps (Girdhar et al., 2022) (Norm Disp)[we set the camera baseline and focal length constant to keep metric depth in the disparity maps], and normalization (Norm) with some mean $\pm$ std. Each model (rows) is trained by its training settings with our VD pipeline. Norm  $2.4\pm.8$  and Norm  $21\pm6$  are derived from the training dataset given their max distance, while Norm  $5\pm5$  is set by us since it encodes most values in to the commonly used encoding values between -1:1. We benchmark the each method on four datasets w.r.t their mean AUC RMSE, which measures the average AUC for RMSE on 1:5:96% of the original depth.  $^\dagger$  The Void(Wong et al., 2020) is not part of the training distribution. Below each dataset we mark their individual depth distribution to highlight model flexibility and to put the RMSE in perspective. Additionally to the depth encoding methods, we also benchmark our methods w.r.t different pretrained weights (Pre-).  $^*$ . We put our ablation results in perspective of the SOTA RGBD encoder Omnivore-B (Girdhar et al., 2022). Here we train our depth completion decoder with our VD pipeline on top of the original Omnivore RGBD encoder to be able to compare against its depth completion capabilities.

		Encoder Specifications			VD Training Settings		Task: Depth Completion (lower is better)				
		Depth Encoding Method	PDE Global $Max_d$	Frozen Encoder		Dataset Max Depth	Metric: mean AUC RMSE [mm]				
RGBD Encoder				RGB	D		Cityscapes	NYUv2	Void $^\dagger$	LM	
Baselines	2×Vit-B	DinoV2	Norm Disp.	-	✓	-	15m	3765.0	139.1	63.0	82.6
	2×Vit-B	DinoV2	Norm $2.4\pm.8$	-	✓	-	15m	3761.7	133.4	63.2	78.78
	2×Vit-B	DinoV2	Norm $5\pm5$	-	✓	-	15m	3652.6	129.8	61.7	76.4
	2×Vit-B	DinoV2	Norm $21\pm6$	-	✓	-	500m	3840.8	156.8	82.3	91.0
With PDE	2×Vit-B	DinoV2	PDE Ch.=16	-	✓	-	500m	3145.6	120.3	60.2	78.0
	2×Vit-B	DinoV2	PDE Ch.=32	-	✓	-	500m	2974.0	113.8	59.4	77.4
	2×Vit-B	DinoV2	PDE Ch.=64	-	✓	-	500m	<b>2940.9</b>	113.4	61.9	76.6
	2×Vit-B	DinoV2	PDE Ch.=32	-	✓	-	15m	3060.1	101.0	45.4	64.5
	2×Vit-B	DinoV2	PDE Ch.=64	-	✓	-	15m	3024.7	97.4	43.6	62.3
	2×Vit-B	DinoV2	PDE Ch.=32	✓	✓	-	15m	3041.8	95.3	40.5	60.1
	2×Vit-B	DinoV2	PDE Ch.=64	✓	✓	-	15m	2995.6	<b>94.4</b>	<b>40.2</b>	<b>59.4</b>
Pre-	2×Vit-B	EVA-02	PDE Ch.=32	✓	✓	-	15m	3216.4	102.6	42.3	63.8
	2×Vit-B	-	PDE Ch.=32	✓	✓	-	15m	3548.4	119.1	52.0	71.3
	Swin3D-B	Omnivore $^*$	Norm Disp.	-	✓	✓	15m	7302.0	609.6	309.7	261.8

sensors with random noise; B) mimic the flickering of time of light depth sensors with perlin noise. We randomly remove between 1 and 99% of the depth input. This enables the depth encoder to handle any depth density.

### 3.3. Multi-Scale Balanced Scale-Invariant Loss

The scale-invariant loss introduced by (Eigen et al., 2014) is commonly used in depth completion. Traditionally, this loss is applied to predicted depth values where no input is present. However, our objective is to be equally good at reconstructing given input pixels and predicting missing input pixels. Since we further randomize the depth input density (see Sec. 3.2), we balance our loss between each sample’s masked scale-invariant reconstruction and prediction loss. This stabilizes training, as both the easy depth reconstruction and the hard depth prediction become equally important, regardless of the depth density distribution in the training batch. Moreover, we use multi-scale depth decoding to ensure hierarchical depth encoding and RGB feature alignment all the way down the depth encoder, which might otherwise be committed due to skip connections for the decoder. *See our supplements for full details of the implementation.*

## 4. Experiments

Following the generalized RGB vision encoders EVA02 (Fang et al., 2024) (MiM-pretrained) and DinoV2 (Oquab et al., 2023), we use ViTs (Dosovitskiy et al., 2020) with image patch size 14 for both our RGB and Depth encoder. We use Vit-B as most methods support this model size and larger models should not fit the high frequency and low latency requirements in robotics. For gradual intermediate RGBD fusion we use a simple S&E (Hu et al., 2017) to combine RGB and Depth signals at the layers [3, 6, 9, 12] (similar to (Ranftl et al., 2021)). The fused RGBD signals are then forwarded to the subsequent depth layer, respectively. We initialize both the RGB and Depth encoder with pretrained RGB encoder weights, since the depth encoder also gets fused RGB embeddings. We keep pretrained RGB encoders frozen during training. This design allows us to leverage the pretrained RGB encoder without corrupting it. For pixel-wise decoding we once again use the RGBD fused attention maps at layers [3, 6, 9, 12] and bilinear resize them for a U-Net decoder (Ronneberger et al., 2015) with four FPN (Lin et al., 2016) heads for multi-scale decoding. For metric depth decoding, we use a lightweight implementation inspired by Adabins (Bhat et al., 2020). Given the max depth  $max_d$ , we

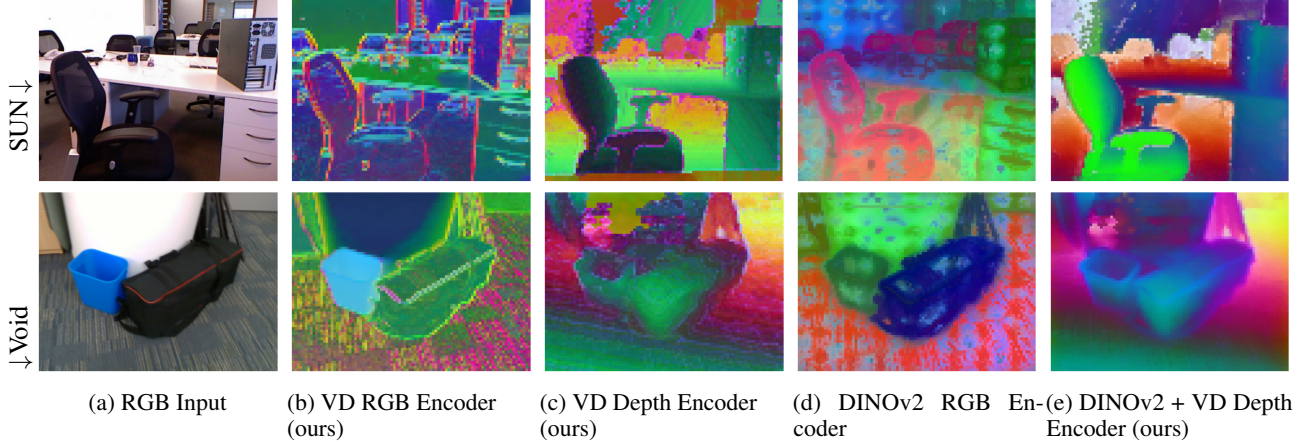


Figure 3. **Visualization of Embeddings:** Following DINOV2 we use PCA to reduce embedded attention maps to three channels (RGB).

decode a vector of length  $n$  per depth index  $j$  from which we compute the final depth  $d_j$  by  $d_j = f(\sum_i^n \frac{max_d}{10i})$ , where  $\frac{max_d}{10n} > 1mm$  and  $f$  is a leaky ReLU activation to avoid and recover from negative outcomes. This stabilizes the decoding as most of the decoded values are within  $\pm 1$ .

#### 4.1. Training Data, Settings, and Ablation

We train our models with the datasets listed in our *supplements* for 100 epochs with our multi-scale balanced scale-invariant loss (Eigen et al., 2014). Each epoch consists of 20k samples drawn evenly from the datasets. We use adam optimization with a batch size of 128 at resolution 224 and a learning rate of 1e-5. We employ image augmentations of color jitter, random gray scale, flips, rotation, and our random depth. In our **ablation study**, we report the mean AUC of the commonly used RMSE metric on multiple datasets (see Tab. 1). We train four baselines each with different norm-based depth encoding. We compare these with different PDE implementations, each with individual  $max_d$ ,  $Ch.$ , and pretrained RGB weights. Following (Vaswani et al., 2017) we use  $Ch. = 64$ , and compare it with the 32 and 16 channel versions, which are lightweight but less precise (*see our supplements for details*). In addition, we perform experiments with different SOTA pretrained encoders and for  $max_d = Max(D)$ , 15m, and 500m. We selected 15m because most indoor depth cameras are bound to around that number, and 500m for extreme outdoor tasks. The results show that our PDE-based encoders yield the best performance with respect to a set of sparse to dense depth completion tasks. Moreover, while  $max_d = Max(D)$  achieves the best results on large distances, we find that fixing the PDE to 15m and rescale large distances is nearly as good. Likewise, we see that 32 channels are sufficient for PDE-based encoding in the 15m range. For further qualitative assessment of our methods, we visualize the attention maps of our best model in Fig. 3. *More visualizations and studies*

on PDE vs. can be found in our supplements.

## 5. Results on Downstream Tasks

We validate the ability of our trained RGBD encoder to extract valuable features for a wide array of downstream tasks. Following DinoV2, we finetune our methods on a resolution of 448p for better adaptation to larger resolutions. We mark our work with +VD(PDE), +VD(P3DE), and +VD(Norm). Here we refer to our VD with: PDE implementation with  $Ch.=32$  and fix global max depth of  $max_d = 15m$ ; the same again for P3DE but with point cloud encoding (see Sec. 3.1); and Norm with depth normalization of  $5 \pm 5$ , respectively. We use PDE with 32 channels because it is more lightweight and nearly as precise as with 64 channels, and  $max_d = 15m$  and norm  $5 \pm 5$  as they again more precise and suits most RGBD downstream tasks. We compare our work with the generalized SOTA RGBD encoders Omnivore (Girdhar et al., 2022), OmniVec (Srivastava & Sharma, 2023), and Omnivec2 (Srivastava & Sharma, 2024) in terms of their ability to adapt to unseen problems without finetuning ("G. RGBD SOTA" in our results). We also report their finetuning results for better classification and put all results in perspective of their absolute SOTA. We train baselines on each RGB encoder and compare them to their RGBD counterparts. We refer to these experiments as "RGB Baselines" and "With RGBD". Omnivore, OmniVec, and Omnivec2 report only results for a small number of RGBD downstream tasks. Therefore, we train more downstream tasks on their encoders with our implementation for a complete, fair, and comprehensive comparison. However, OmniVec and OmniVec2 have not yet shared their implantation and models, hindering us from including them in our RGB baseline and RGBD experiments. *Please find the full implementation specification for the downstream tasks, their respective datasets, and omnivore in our supplements.*

**Table 2. Depth Completion Results:** We test the depth completion precision of the VD trained on related unseen datasets. We put the results into perspective of the respective absolute published SOTA of: 709.41 (Nazir et al., 2022), 216.50 (Jeon et al., 2022), 195.32 (Wong et al., 2020), and 95.86 (Wong & Soatto, 2021). We trained our decoder with our VD pipeline on top of the original Omnivore (Girdhar et al., 2022) to compare against its depth completion capabilities. \* TBA due to Kitti test server allows max 3 tests per month.

		Task & Metric →	Depth Completion (RMSE)				
		Dataset →	Kitti		Void		
		Data Split →	Test	Valid	150	500	1500
		Resolution →	1216 × 352		640 × 480		
		Max Depth →	80m		5m		
		Depth Mean±STD →	16.12±11.86		1.65±.99		
		Available Depth →	5%		0.05%	0.15%	0.5%
		Absolute SOTA →	709.41	-	216.50	195.32	95.86
RGBD	Swin3D-B	Omnivore	-*	8301.7	787.3	835.1	738.1
	2×Vit-B	VD(PDE) [Ours]	1695.51	1698.9	297.8	244.2	161.9
	2×Vit-B	EVA-02 +VD(PDE) [Ours]	1626.22	1649.5	195.5	160.2	117.2
	2×Vit-B	DinoV2 +VD(PDE) [Ours]	<b>1625.06</b>	<b>1646.9</b>	<b>134.8</b>	<b>111.8</b>	<b>88.3</b>
	2×Vit-B	DinoV2 +VD(Norm) [Ours]	-*	5.2594	1.1562	1.1656	1.144

**Table 3. Classification Results:** We train a fully-connected classification layer on top of the frozen encoders (pretrained by their respective methods) for the given set of related datasets. We compare the "RGB Baselines" vs. the related generalized RGBD SOTA ("G. RGBD SOTA"), and vs. "with RGBD" implementations. We put the results into perspective of the respective absolute published SOTA of: 75.9! (Srivastava & Sharma, 2024) , 80.3 (Girdhar et al., 2022), 91.1 (Chen et al., 2023), 94.6 (Srivastava & Sharma, 2024). \*Omnivore reports their KNN based classification given the inputs of RGB, Depth, and RGBD, respectively. Note that original Omnivore reports the ability to process depth, but loses performance when adding depth to the basic RGB input. Our results further confirm this. † is using the depth encoder but without depth. This is to achieve a better comparability w.r.t training settings, segmentation head implementation, and closing gaps on missing datasets. ! OmniVec (Srivastava & Sharma, 2023) and OmniVec2 (Srivastava & Sharma, 2024) have not yet published their models and implementation, hindering us to include them into our baseline and RGBD experiments.

		Task →	Scene Classification		Object Classification	
		Dataset →	NYUv2	SUN-RGBD	ImageNet	MVIP
Encoder	Method ↓	Absolute SOTA →	80.3	75.9 !	91.1	94.6
RGB Baselines	SWin3D-B	Omnivore	81.5	67.2	<u>84.9</u>	66.0
	Vit-B	VD(PDE) [Ours]	33.5	23.8	10.5	23.0
	2×Vit-B	VD(PDE) [Ours] <sup>†</sup>	32.7	22.3	12.2	24.1
	Vit-B	EVA-02	83.2	68.3	80.2	49.7
	Vit-B	DINOv2	82.7	<u>70.4</u>	84.0	<b>77.4</b>
G. RGBD SOTA	Swin3D-B	Omnivore	-	67.2	84.3, 63.1, 83.7*	15.42
	Swin3D-B	Omnivore(Finetuned)	80.3	-	-	-
	BERT	OmniVec !	-	71.4	88.6	-
	BERT	OmniVec(Finetuned) v!	-	74.6	92.4	-
	BERT	OmniVec2 !	-	74.6	89.3	-
	BERT	OmniVec2(Finetuned) !	-	<b>75.9</b>	<b>93.6</b>	-
With RGBD	Swin3D-B	Omnivore	81.7	62.5	81.0	64.7
	2×Vit-B	VD(PDE) [Ours]	43.9	27.9	15.4	12.6
	2×Vit-B	EVA-02 +VD(PED) [Ours]	82.3	67.6	78.7	42.2
	2×Vit-B	DinoV2 +VD(PDE) [Ours]	83.0	70.2	83.8	71.0
	2×Vit-B	DinoV2 +VD(Norm) [Ours]	<b>83.8</b>	68.8	83.56	<u>75.1</u>

## 5.1. Depth Completion

We test the encoder-decoder models trained with VD on the unseen Kitti (Geiger et al., 2012) and Void (Wong et al.,

2020). In Tab. 2 we summarize our results in which we achieve the SOTA on Void. Here we observe that Omnivore does not yield precise metric depth embeddings. In addition

**Table 4. Segmentation Results:** We train a mask2former (Cheng et al., 2022) segmentation head on top of the frozen encoders (pretrained by their respective methods) for the given set of related datasets. We compare the "RGB Baselines" vs. the related generalized RGBD SOTA ("G. RGBD SOTA"), and vs. "with RGBD" implementations. We put the results into perspective of the respective absolute published SOTA of: 63.6! (Srivastava & Sharma, 2024), 54.6 (Jia et al., 2024), 87.35 (Erisen, 2024), 62.8 (Wang et al., 2022a), and 53.4 (Fang et al., 2022). \* we generate depth data with UniDepth (Piccinelli et al., 2024) as these datasets do not have depth data. As such the depth data is inconsistent and occasionally very wrong. <sup>†</sup> is using the depth encoder but without depth. ! OmniVec (Srivastava & Sharma, 2023) and OmniVec2 (Srivastava & Sharma, 2024) have not yet published their models and implementation, hindering us to include them into our baseline and RGBD experiments.

		Task→	Semantic Segmentation				
		Metric→	mean Intersection over Union (mIoU)				
		Depth Origin→	Captured by Depth Sensors			Monocular Depth Estimation	
		Dataset→	NYUv2	SUN-RGBD	Cityscapes	ADE20K*	Coco-Stuff*
Encoder	Method↓	Absolute SOTA→	63.6 !	54.6	87.35	62.8	53.4
RGB Baselines	Swin3D-B	Omnivore	43.48	46.49	71.77	45.93	42.70
	Vit-B	EVA-02	30.14	39.05	48.37	32.71	28.66
	Vit-B	DINOv2	52.69	53.75	74.42	51.72	44.55
	Vit-B	VD(PDE) [Ours]	20.02	31.56	52.53	25.32	19.79
	2×Vit-B	VD(PDE) [Ours] <sup>†</sup>	22.39	32.12	57.16	29.54	23.79
G. RGBD SOTA	Swin3D-B	Omnivore(Finetuned)	56.8	-	-	-	-
	BERT	OmniVec !	58.6	-	-	-	-
	BERT	OmniVec(Finetuned) !	60.8	-	-	-	-
	BERT	OmniVec2 !	62.5	-	-	-	-
	BERT	OmniVec2(Finetuned) !	<b>63.6</b>	-	-	<b>58.5</b>	-
With RGBD	Swin3D-B	Omnivore	42.28	40.93	60.96	44.32	41.88
	2×Vit-B	VD(PDE) [Ours]	29.61	38.04	60.63	36.60	29.66
	2×Vit-B	EVA-02 +VD(PDE) [Ours]	38.05	44.06	66.46	43.49	39.57
	2×Vit-B	DinoV2 +VD(PDE) [Ours]	54.81	<b>56.05</b>	<b>77.26</b>	53.41	<b>49.91</b>
	2×Vit-B	DinoV2 +VD(Norm) [Ours]	<b>55.07</b>	55.80	77.05	<b>53.57</b>	49.52

to depth completion results, these experiments further show that PDE yield more precise and stable depth encoding than norm-based methods. This is especially true for sparse depth inputs, which PDE handles relatively well, but our Norm-based encoder has a lot of trouble with. *See our supplements for further studies on PDE vs. Norm-based depth encoding.*

## 5.2. Classification

VD does not aim for image classification-specific feature extraction. Moreover, we do not think that RGBD is especially useful for image classification. However, we follow the likes of Omnivore and report our classification results in Tab. 3 for NYUv2 (Silberman et al., 2012) and SUN-RGBD (Song et al., 2015). We extend the investigation to ImageNet-1k (Deng et al., 2009) and MVIP (Koch et al., 2023) to include object classification. Although depth is value adding for our models without a pretrained RGB encoder, we can only see some minor improvements to the RGB baselines, and sometimes even negative impact. Also, the results do not favor either PDE- or norm-based depth encoding. For Omnivore, we can reproduce and even improve some of their results with our training pipeline (*see our sup-*

*plements*). Unlike our encoders, we find that Omnivore's RGBD results are significantly negatively affected when compared to their RGB baseline. This aligns with their own findings on KNN based ImageNet-1k classification.

## 5.3. Segmentation

Using MMSegmentation (Contributors, 2020) we train a commonly used mask2former (Cheng et al., 2022) segmentation head on top of our frozen encoders for NYUv2 (Silberman et al., 2012), SUN-RGBD (Song et al., 2015), Cityscapes (Cordts et al., 2016), ADE20k (Zhou et al., 2017), and COCO-Stuff (Caesar et al., 2016) datasets. In Tab. 4 we summarize our segmentation results, where we are able to reach SOTA results of 56.05 mIoU on SUN-RGBD. Unlike our results, we observe again that the raw pretrained Omnivore without finetuning gets negatively affected when incorporation depth. *We further analyze the depth-encoding stability of our methods and Omnivore on SUN-RGBD in our supplements*. There, we investigate the effect of changing the depth distribution and density, which causes major problems for Omnivore but not for our depth encoders. With respect to PDE vs. norm-based depth encoding, we can not

**Table 5. Pose Estimation Results:** We train a PoET(GT) (Jantos et al., 2022) 6D object pose estimation head on top of the frozen encoders (pretrained by their respective methods) for the given set of related datasets. We report the by respective commonly used AUC ADD(S) (Xiang et al., 2017), AR (Hodan et al., 2024), and ADD-S (Hinterstoisser et al., 2013). We compare the RGB Baselines vs. original PoET (Jantos et al., 2022), and vs. RGBD specific implementations. We put the results into perspective of the respective absolute published SOTA of: 95.43 (Wang et al., 2023), 71.1 (Wu et al., 2021), and AR (Hodan et al., 2024). \* for AR we use the Bop (Hodan et al., 2024) test selection of the datasets. †For HB (Kaskman et al., 2019) we use the validation Bop (Hodan et al., 2024) selection, since the test selection has no public ground truth masks and bounding boxes, which are required by PoET(GT) (Jantos et al., 2022). The training and val set are of the same data distribution and as such comparable the proportions of the metric results.

			Task→	6D Object Pose Estimation							
			Dataset→	YCB-Video		HomeBrew				LM-O	
			Metric→	AUC	AR*	AUC	AR*	AUC	ADD-S	AR*	
			Absolute SOTA→	95.43	92.9	-	95.6	-	71.1	80.5†	
Encoder	Method↓	Original PoET(GT)→		92.8	68.3	-	-	-	36.8	-	
RGB Baselines	Swin3D-B	Omnivore		65.23	43.22	43.58	28.86	46.14	14.54	25.60	
	Vit-B	EVA-02		64.49	46.49	37.23	22.19	63.54	25.50	<b>41.94</b>	
	Vit-B	DINOv2		71.17	57.96	41.28	34.67	54.81	20.30	41.24	
With RGBD	Swin3D-B	Omnivore		59.20	35.06	41.56	14.58	55.33	22.98	33.60	
	2×Vit-B	EVA-02 +VD(PDE) [Ours]		77.13	56.27	60.68	44.25	63.13	27.60	36.59	
	2×Vit-B	DinoV2 +VD(PDE) [Ours]		81.81	63.04	<b>67.07</b>	<b>53.24</b>	64.47	29.76	36.59	
	2×Vit-B	DinoV2 +VD(P3DE) [Ours]		<b>83.87</b>	<b>70.64</b>	66.25	52.20	<b>64.73</b>	<b>30.46</b>	41.18	
	2×Vit-B	DinoV2 +VD(Norm) [Ours]		83.41	65.23	63.82	46.94	64.49	29.41	40.84	

observe much of a difference in segmentation tasks.

#### 5.4. 6D Object Pose Estimation

Note, that Omnivore, OmniVec, and OmniVec2 do not address 6D pose estimation. We believe that robotic applications are most relevant for precise depth encoders. Therefore, we train a PoET (Jantos et al., 2022) 6D object pose estimation head on top of our frozen encoders for YCV-Video, Homebrew, and LM-O from BoP. PoET follows the generalized decoder architecture of Deformable-DeTR (Zhu et al., 2021) and is applicable to any encoder. PoET works without any data-oriented tailored design or post-process, which makes it a perfect fit to analyze and compare the encoders’ generalization and adaptability. For pose estimation as we also investigate our P3DE-based encoder as 3D becomes relevant in this task. In Tab. 5 we summarize our results on YCB-Video(Xiang et al., 2017), HomeBrew (Kaskman et al., 2019), and LM-O (Brachmann et al., 2014). Here, one can see the most significant impact of our VD encoders with respect to their baselines. Omnivore is again negatively affected by RGBD for all datasets but LM-O, which is the opposite for the VD encoders regarding the AR metric. These AR results on LM-O (known for high object occlusion) might indicate that high occlusion could decrease the importance of depth precision. However, these speculations require further research. Eventually, PDE again proves to be more resilient than norm-based depth encoding on average, although not constantly. The same can be observed for P3DE with minor improvements.

## 6. Conclusion

We present Vanishing Depth, a novel self-supervised learning pipeline to augment existing generalized RGB image encoders to incorporate depth feature extraction into their embeddings. Our depth augmented RGBD encoders demonstrate a general capability to solve related RGBD downstream tasks, without further fine-tuning and on various depth distributions and densities. In addition, they exceed the RGB baselines of their predecessors and SOTA competitors on various downstream benchmarks. Notably, we achieve SOTA with 56.05 mIoU on SUN-RGBD segmentation and 88.3 RMSE on Void’s depth completion. Moreover, in pose estimation, our depth-augmented encoders outperform their predecessors and competitors by a large margin in most metrics. This underlies the value of our methods’ generalized RGBD feature extraction. With our PDE, we archive a higher precision than using norm-based depth encoding. This is particularly evident in our depth completion results. Although norm-based VD encoders yield good and sometimes better results than the PDE-based counterparts, we further show in our supplements that PDE is generally more stable and less affected by the input depth distribution and especially depth density. Our work contributes to research for generalized multi-modal image encoders, which enables generalization on various domains, distributions, densities, problem sizes, and downstream tasks. This is achieved without the need for finetuning, allowing for fast adaptation on a shared encoder for efficient and modular multi-agent systems.

## References

Bao, H., Dong, L., and Wei, F. Beit: BERT pre-training of image transformers. *CoRR*, abs/2106.08254, 2021. URL <https://arxiv.org/abs/2106.08254>.

Bhat, S. F., Alhashim, I., and Wonka, P. Adabins: Depth estimation using adaptive bins. *CoRR*, abs/2011.14141, 2020. URL <https://arxiv.org/abs/2011.14141>.

Bommasani, R., Hudson, D. A., Adeli, E., Altman, R. B., Arora, S., von Arx, S., Bernstein, M. S., Bohg, J., Bosselet, A., Brunskill, E., Brynjolfsson, E., Buch, S., Card, D., Castellon, R., Chatterji, N. S., Chen, A. S., Creel, K., Davis, J. Q., Demszky, D., Donahue, C., Doumbouya, M., Durmus, E., Ermon, S., Etchemendy, J., Ethayarajh, K., Fei-Fei, L., Finn, C., Gale, T., Gillespie, L., Goel, K., Goodman, N. D., Grossman, S., Guha, N., Hashimoto, T., Henderson, P., Hewitt, J., Ho, D. E., Hong, J., Hsu, K., Huang, J., Icard, T., Jain, S., Jurafsky, D., Kalluri, P., Karamcheti, S., Keeling, G., Khani, F., Khatbab, O., Koh, P. W., Krass, M. S., Krishna, R., Kuditipudi, R., and et al. On the opportunities and risks of foundation models. *CoRR*, abs/2108.07258, 2021. URL <https://arxiv.org/abs/2108.07258>.

Brachmann, E., Krull, A., Michel, F., Gumhold, S., Shotton, J., and Rother, C. Learning 6d object pose estimation using 3d object coordinates. In Fleet, D., Pajdla, T., Schiele, B., and Tuytelaars, T. (eds.), *Computer Vision – ECCV 2014*, pp. 536–551, Cham, 2014. Springer International Publishing. ISBN 978-3-319-10605-2.

Brown, T. B., Mann, B., Ryder, N., Subbiah, M., Kaplan, J., Dhariwal, P., Neelakantan, A., Shyam, P., Sastry, G., Askell, A., Agarwal, S., Herbert-Voss, A., Krueger, G., Henighan, T., Child, R., Ramesh, A., Ziegler, D. M., Wu, J., Winter, C., Hesse, C., Chen, M., Sigler, E., Litwin, M., Gray, S., Chess, B., Clark, J., Berner, C., McCandlish, S., Radford, A., Sutskever, I., and Amodei, D. Language models are few-shot learners. *CoRR*, abs/2005.14165, 2020. URL <https://arxiv.org/abs/2005.14165>.

Caesar, H., Uijlings, J. R. R., and Ferrari, V. Coco-stuff: Thing and stuff classes in context. *CoRR*, abs/1612.03716, 2016. URL <http://arxiv.org/abs/1612.03716>.

Caron, M., Touvron, H., Misra, I., Jégou, H., Mairal, J., Bojanowski, P., and Joulin, A. Emerging properties in self-supervised vision transformers. *CoRR*, abs/2104.14294, 2021. URL <https://arxiv.org/abs/2104.14294>.

Chang, A. X., Dai, A., Funkhouser, T. A., Halber, M., Nießner, M., Savva, M., Song, S., Zeng, A., and Zhang, Y. Matterport3d: Learning from RGB-D data in indoor environments. *CoRR*, abs/1709.06158, 2017. URL <http://arxiv.org/abs/1709.06158>.

Chen, X., Liang, C., Huang, D., Real, E., Wang, K., Liu, Y., Pham, H., Dong, X., Luong, T., Hsieh, C.-J., Lu, Y., and Le, Q. V. Symbolic discovery of optimization algorithms, 2023.

Cheng, B., Misra, I., Schwing, A. G., Kirillov, A., and Girdhar, R. Masked-attention mask transformer for universal image segmentation, 2022. URL <https://arxiv.org/abs/2112.01527>.

Contributors, M. MM Segmentation: Openmmlab semantic segmentation toolbox and benchmark. <https://github.com/open-mmlab/mmsegmentation>, 2020.

Cordts, M., Omran, M., Ramos, S., Rehfeld, T., Enzweiler, M., Benenson, R., Franke, U., Roth, S., and Schiele, B. The cityscapes dataset for semantic urban scene understanding. *CoRR*, abs/1604.01685, 2016. URL <http://arxiv.org/abs/1604.01685>.

Dai, A., Chang, A. X., Savva, M., Halber, M., Funkhouser, T. A., and Nießner, M. Scannet: Richly-annotated 3d reconstructions of indoor scenes. *CoRR*, abs/1702.04405, 2017. URL <http://arxiv.org/abs/1702.04405>.

Deng, J., Dong, W., Socher, R., Li, L.-J., Li, K., and Fei-Fei, L. Imagenet: A large-scale hierarchical image database. In *2009 IEEE conference on computer vision and pattern recognition*, pp. 248–255. Ieee, 2009.

Dosovitskiy, A., Beyer, L., Kolesnikov, A., Weissenborn, D., Zhai, X., Unterthiner, T., Dehghani, M., Minderer, M., Heigold, G., Gelly, S., Uszkoreit, J., and Houlsby, N. An image is worth 16x16 words: Transformers for image recognition at scale. *CoRR*, abs/2010.11929, 2020. URL <https://arxiv.org/abs/2010.11929>.

Eigen, D. and Fergus, R. Predicting depth, surface normals and semantic labels with a common multi-scale convolutional architecture. *CoRR*, abs/1411.4734, 2014. URL <http://arxiv.org/abs/1411.4734>.

Eigen, D., Puhrsch, C., and Fergus, R. Depth map prediction from a single image using a multi-scale deep network. *CoRR*, abs/1406.2283, 2014. URL <http://arxiv.org/abs/1406.2283>.

El-Nouby, A., Izacard, G., Touvron, H., Laptev, I., Jégou, H., and Grave, E. Are large-scale datasets necessary for self-supervised pre-training? *CoRR*, abs/2112.10740, 2021. URL <https://arxiv.org/abs/2112.10740>.

Erisen, S. Sernet-former: Semantic segmentation by efficient residual network with attention-boosting gates and attention-fusion networks. 2024. doi: 10.48550/ARXIV.2401.15741. URL <https://arxiv.org/abs/2401.15741>.

Fang, H.-S., Wang, C., Gou, M., and Lu, C. Graspnet-1billion: A large-scale benchmark for general object grasping. In *Proceedings of the IEEE/CVF Conference on Computer Vision and Pattern Recognition*, pp. 11444–11453, 2020.

Fang, Y., Wang, W., Xie, B., Sun, Q., Wu, L., Wang, X., Huang, T., Wang, X., and Cao, Y. Eva: Exploring the limits of masked visual representation learning at scale. *arXiv preprint arXiv:2211.07636*, 2022.

Fang, Y., Sun, Q., Wang, X., Huang, T., Wang, X., and Cao, Y. Eva-02: A visual representation for neon genesis. *Image and Vision Computing*, pp. 105171, 2024.

Gansbeke, W. V., Neven, D., Brabandere, B. D., and Gool, L. V. Sparse and noisy lidar completion with RGB guidance and uncertainty. *CoRR*, abs/1902.05356, 2019. URL <https://arxiv.org/abs/1902.05356>.

Geiger, A., Lenz, P., and Urtasun, R. Are we ready for autonomous driving? the kitti vision benchmark suite. In *2012 IEEE Conference on Computer Vision and Pattern Recognition*, pp. 3354–3361, 2012. doi: 10.1109/CVPR.2012.6248074.

Girdhar, R., Singh, M., Ravi, N., van der Maaten, L., Joulin, A., and Misra, I. Omnivore: A single model for many visual modalities. *CoRR*, abs/2201.08377, 2022. URL <https://arxiv.org/abs/2201.08377>.

Gupta, S., Girshick, R. B., Arbelaez, P., and Malik, J. Learning rich features from RGB-D images for object detection and segmentation. *CoRR*, abs/1407.5736, 2014. URL <https://arxiv.org/abs/1407.5736>.

He, K., Chen, X., Xie, S., Li, Y., Dollár, P., and Girshick, R. B. Masked autoencoders are scalable vision learners. *CoRR*, abs/2111.06377, 2021. URL <https://arxiv.org/abs/2111.06377>.

Hinterstoisser, S., Lepetit, V., Ilic, S., Holzer, S., Bradski, G., Konolige, K., and Navab, N. Model based training, detection and pose estimation of texture-less 3d objects in heavily cluttered scenes. In Lee, K. M., Matsushita, Y., Rehg, J. M., and Hu, Z. (eds.), *Computer Vision – ACCV 2012*, pp. 548–562, Berlin, Heidelberg, 2013. Springer Berlin Heidelberg. ISBN 978-3-642-37331-2.

Hodan, T., Haluza, P., Obdrzálek, S., Matas, J., Lourakis, M. I. A., and Zabulis, X. T-LESS: an RGB-D dataset for 6d pose estimation of texture-less objects. *CoRR*, abs/1701.05498, 2017. URL <http://arxiv.org/abs/1701.05498>.

Hodan, T., Sundermeyer, M., Labbe, Y., Nguyen, V. N., Wang, G., Brachmann, E., Drost, B., Lepetit, V., Rother, C., and Matas, J. Bop challenge 2023 on detection, segmentation and pose estimation of seen and unseen rigid objects, 2024. URL <https://arxiv.org/abs/2403.09799>.

Hondru, V., Croitoru, F. A., Minaee, S., Ionescu, R. T., and Sebe, N. Masked image modeling: A survey, 2025. URL <https://arxiv.org/abs/2408.06687>.

Hu, J., Shen, L., and Sun, G. Squeeze-and-excitation networks. *CoRR*, abs/1709.01507, 2017. URL <http://arxiv.org/abs/1709.01507>.

Hu, M., Wang, S., Li, B., Ning, S., Fan, L., and Gong, X. Penet: Towards precise and efficient image guided depth completion. *CoRR*, abs/2103.00783, 2021. URL <https://arxiv.org/abs/2103.00783>.

Jantos, T., Hamdad, M. A., Granig, W., Weiss, S., and Steinbrenner, J. Poet: Pose estimation transformer for single-view, multi-object 6d pose estimation, 2022.

Jaritz, M., de Charette, R., Wirbel, É., Perrotton, X., and Nashashibi, F. Sparse and dense data with cnns: Depth completion and semantic segmentation. *CoRR*, abs/1808.00769, 2018. URL <http://arxiv.org/abs/1808.00769>.

Jeon, J., Lim, H., Seo, D.-U., and Myung, H. Struct-mdc: Mesh-refined unsupervised depth completion leveraging structural regularities from visual slam, 2022. URL <https://arxiv.org/abs/2204.13877>.

Jia, D., Guo, J., Han, K., Wu, H., Zhang, C., Xu, C., and Chen, X. Geminifusion: Efficient pixel-wise multimodal fusion for vision transformer, 2024. URL <https://arxiv.org/abs/2406.01210>.

Kaskman, R., Zakharov, S., Shugurov, I., and Ilic, S. Homebreweddb: RGB-D dataset for 6d pose estimation of 3d objects. *CoRR*, abs/1904.03167, 2019. URL <http://arxiv.org/abs/1904.03167>.

Koch, P., Schlüter, M., and Briese, C. Mvip: A dataset for industrial part recognition, 2023.

Lahoud, J. and Ghanem, B. Rgb-based semantic segmentation using self-supervised depth pre-training. *CoRR*, abs/2002.02200, 2020. URL <https://arxiv.org/abs/2002.02200>.

Li, L. and Heizmann, M. A closer look at invariances in self-supervised pre-training for 3d vision, 2022.

Lin, T., Dollár, P., Girshick, R. B., He, K., Hariharan, B., and Belongie, S. J. Feature pyramid networks for object detection. *CoRR*, abs/1612.03144, 2016. URL <http://arxiv.org/abs/1612.03144>.

Liu, H., Li, C., Wu, Q., and Lee, Y. J. Visual instruction tuning, 2023. URL <https://arxiv.org/abs/2304.08485>.

Mukhoti, J., Gal, Y., Torr, P. H. S., and Dokania, P. K. Fine-tuning can cripple your foundation model; preserving features may be the solution, 2024. URL <https://arxiv.org/abs/2308.13320>.

Nazir, D., Liwicki, M., Stricker, D., and Afzal, M. Z. Semmatnet: Towards attention-based semantic aware guided depth completion, 2022.

Ning, J., Li, C., Zhang, Z., Geng, Z., Dai, Q., He, K., and Hu, H. All in tokens: Unifying output space of visual tasks via soft token, 2023.

Oquab, M., Dariseti, T., Moutakanni, T., Vo, H., Szafraniec, M., Khalidov, V., Fernandez, P., Haziza, D., Massa, F., El-Nouby, A., Assran, M., Ballas, N., Galuba, W., Howes, R., Huang, P.-Y., Li, S.-W., Misra, I., Rabbat, M., Sharma, V., Synnaeve, G., Xu, H., Jegou, H., Mairal, J., Labatut, P., Joulin, A., and Bojanowski, P. Dinov2: Learning robust visual features without supervision, 2023.

Park, J., Joo, K., Hu, Z., Liu, C., and Kweon, I. S. Non-local spatial propagation network for depth completion. *CoRR*, abs/2007.10042, 2020. URL <https://arxiv.org/abs/2007.10042>.

Pathak, D., Krähenbühl, P., Donahue, J., Darrell, T., and Efros, A. A. Context encoders: Feature learning by inpainting. *CoRR*, abs/1604.07379, 2016. URL <https://arxiv.org/abs/1604.07379>.

Piccinelli, L., Yang, Y.-H., Sakaridis, C., Segu, M., Li, S., Gool, L. V., and Yu, F. Unidepth: Universal monocular metric depth estimation, 2024. URL <https://arxiv.org/abs/2403.18913>.

Radford, A., Kim, J. W., Hallacy, C., Ramesh, A., Goh, G., Agarwal, S., Sastry, G., Askell, A., Mishkin, P., Clark, J., Krueger, G., and Sutskever, I. Learning transferable visual models from natural language supervision. *CoRR*, abs/2103.00020, 2021. URL <https://arxiv.org/abs/2103.00020>.

Ranftl, R., Bochkovskiy, A., and Koltun, V. Vision transformers for dense prediction. *CoRR*, abs/2103.13413, 2021. URL <https://arxiv.org/abs/2103.13413>.

Ronneberger, O., Fischer, P., and Brox, T. U-net: Convolutional networks for biomedical image segmentation. *CoRR*, abs/1505.04597, 2015. URL <http://arxiv.org/abs/1505.04597>.

Seichter, D., Stephan, B., Fischedick, S. B., Müller, S., Rabes, L., and Gross, H.-M. Panopticndt: Efficient and robust panoptic mapping, 2023.

Silberman, N., Hoiem, D., Kohli, P., and Fergus, R. Indoor segmentation and support inference from rgbd images. pp. 746–760, 10 2012. ISBN 978-3-642-33714-7. doi: 10.1007/978-3-642-33715-4\_54.

Song, S., Lichtenberg, S., and Xiao, J. Sun rgb-d: A rgb-d scene understanding benchmark suite. pp. 567–576, 06 2015. doi: 10.1109/CVPR.2015.7298655.

Srivastava, S. and Sharma, G. Omnivec: Learning robust representations with cross modal sharing, 2023. URL <https://arxiv.org/abs/2311.05709>.

Srivastava, S. and Sharma, G. Omnivec2 - a novel transformer based network for large scale multimodal and multitask learning. In *2024 IEEE/CVF Conference on Computer Vision and Pattern Recognition (CVPR)*, pp. 27402–27414, 2024. doi: 10.1109/CVPR52733.2024.02588.

Valada, A., Mohan, R., and Burgard, W. Self-supervised model adaptation for multimodal semantic segmentation. *CoRR*, abs/1808.03833, 2018. URL <http://arxiv.org/abs/1808.03833>.

Vaswani, A., Shazeer, N., Parmar, N., Uszkoreit, J., Jones, L., Gomez, A. N., Kaiser, L., and Polosukhin, I. Attention is all you need. *CoRR*, abs/1706.03762, 2017. URL <http://arxiv.org/abs/1706.03762>.

Wang, W., Bao, H., Dong, L., Bjorck, J., Peng, Z., Liu, Q., Aggarwal, K., Mohammed, O. K., Singhal, S., Som, S., and Wei, F. Image as a foreign language: Beit pretraining for all vision and vision-language tasks, 2022a. URL <https://arxiv.org/abs/2208.10442>.

Wang, Y., Chen, X., Cao, L., Huang, W., Sun, F., and Wang, Y. Multimodal token fusion for vision transformers. In *Proceedings of the IEEE/CVF Conference on Computer Vision and Pattern Recognition (CVPR)*, pp. 12186–12195, June 2022b.

Wang, Z., Sun, X., Wei, H., Ma, Q., and Zhang, Q. Enhancing 6-dof object pose estimation through multiple modality fusion: A hybrid cnn architecture with cross-layer and cross-modal integration. *Machines*, 11(9), 2023. ISSN 2075-1702. doi: 10.3390/machines11090891. URL <https://www.mdpi.com/2075-1702/11/9/891>.

Wong, A. and Soatto, S. Unsupervised depth completion with calibrated backprojection layers. *CoRR*, abs/2108.10531, 2021. URL <https://arxiv.org/abs/2108.10531>.

Wong, A., Fei, X., Tsuei, S., and Soatto, S. Unsupervised depth completion from visual inertial odometry. *IEEE Robotics and Automation Letters*, 5(2):1899–1906, 2020.

Wu, Y., Zand, M., Etemad, A., and Greenspan, M. A. Vote from the center: 6 dof pose estimation in RGB-D images by radial keypoint voting. *CoRR*, abs/2104.02527, 2021. URL <https://arxiv.org/abs/2104.02527>.

Xiang, Y., Schmidt, T., Narayanan, V., and Fox, D. Posecnn: A convolutional neural network for 6d object pose estimation in cluttered scenes. *CoRR*, abs/1711.00199, 2017. URL <http://arxiv.org/abs/1711.00199>.

Yan, Z., Wang, K., Li, X., Zhang, Z., Xu, B., Li, J., and Yang, J. Rignet: Repetitive image guided network for depth completion. *CoRR*, abs/2107.13802, 2021. URL <https://arxiv.org/abs/2107.13802>.

Yao, Y., Luo, Z., Li, S., Zhang, J., Ren, Y., Zhou, L., Fang, T., and Quan, L. Blendedmvs: A large-scale dataset for generalized multi-view stereo networks. *CoRR*, abs/1911.10127, 2019. URL <http://arxiv.org/abs/1911.10127>.

Yin, B., Zhang, X., Li, Z., Liu, L., Cheng, M.-M., and Hou, Q. Dformer: Rethinking rgbd representation learning for semantic segmentation, 2023.

Zhang, J., Liu, H., Yang, K., Hu, X., Liu, R., and Stiefelhagen, R. Cmx: Cross-modal fusion for rgb-x semantic segmentation with transformers, 2023.

Zhao, X., Pang, Y., Zhang, L., Lu, H., and Ruan, X. Self-supervised representation learning for RGB-D salient object detection. *CoRR*, abs/2101.12482, 2021. URL <https://arxiv.org/abs/2101.12482>.

Zhou, B., Zhao, H., Puig, X., Fidler, S., Barriuso, A., and Torralba, A. Scene parsing through ade20k dataset. In *2017 IEEE Conference on Computer Vision and Pattern Recognition (CVPR)*, pp. 5122–5130, 2017. doi: 10.1109/CVPR.2017.544.

Zhou, J., Wei, C., Wang, H., Shen, W., Xie, C., Yuille, A. L., and Kong, T. ibot: Image BERT pre-training with online tokenizer. *CoRR*, abs/2111.07832, 2021. URL <https://arxiv.org/abs/2111.07832>.

Zhu, X., Su, W., Lu, L., Li, B., Wang, X., and Dai, J. Deformable detr: Deformable transformers for end-to-end object detection, 2021. URL <https://arxiv.org/abs/2010.04159>.

## A. Training Specifications

### A.1. Training Data

In Tab. 6 we summarize the data used in your VD training and experiments on downstream tasks. We also highlight the depth distribution and density. This array of datasets is not curated and properly balanced. In future work, we would like to follow the likes of DinoV2 (Oquab et al., 2023) and build a more sophisticated and balanced database for our training.

**Table 6. Training and Test Datasets:** We checkmark the datasets which are used for our vanishing depth (VD) training. The other datasets are used purely in our experiments for benchmark validation on different downstream tasks. Further, we report the mean $\pm$ std and proportion of zeros (missing depth values) within the depth images of the most relevant data splits marked with a star (\*).

Dataset Name		VD	RGBD-Images	Dataset Scenery: Objective	Depth mean [m] & density
Cityscapes (Cordts et al., 2016)		✓	104k*	City Streets: Segmentation	27.7 $\pm$ 26.0 78%
NYU-v2 (Silberman et al., 2012)		✓	482k*	Indoor: Segmentation	4.1 $\pm$ 1.5 86%
YCB-Video (Xiang et al., 2017)		✓	113k*	Objects: 6D-Pose	1.2 $\pm$ 0.5 82%
LM (Hinterstoisser et al., 2013)		✓	50k*	Objects: 6D-Pose	1.1 $\pm$ 0.4 90%
T-Less (Hodan et al., 2017)		✓	50k*	Objects: 6D-Pose	1.0 $\pm$ 0.4 92%
GraspNet (Fang et al., 2020)		✓	51*	Robot Cell: Grasping-Pose	0.5 $\pm$ 0.2 90%
ScanNet (Dai et al., 2017)		✓	2 477k	Indoor: Segmentation	1.8 $\pm$ 0.5 100%
MatterPort3D (Chang et al., 2017)		✓	194k	Indoor: Segmentation	2.0 $\pm$ 0.7 100%
BlendedMVS (Yao et al., 2019)		✓	48k	Landscapes: Multi-View Stereo	83.4 $\pm$ 24.7 100%
Kitti (Geiger et al., 2012)		-	7k	City & Streets Depth Estimation	15.7 $\pm$ 11.5 16%
SUN-RGBD (Song et al., 2015)		-	5k	Indoor: Segmentation	2.3 $\pm$ 0.7 87%
Void (Wong et al., 2020)		-	59k	Indoor: Depth Completion	1.65 $\pm$ 0.99 96%
HomeBrew (Kaskman et al., 2019)		-	50k	Indoor: Synt2Real 6D-Pose	1.25 $\pm$ 0.94 84%
MVIP (Koch et al., 2023)		-	37k	Industrial: Classification	0.91 $\pm$ 0.88 85%
LM-O (Brachmann et al., 2014)		-	50k*	Objects: 6D-Pose	1.1 $\pm$ 0.4 90%

### A.2. Positional Depth Encoding

For our ablation study and other experiments we use the PDE with 64, 32, and 16 channels. We keep a constant temperature of 3e-4, encoding the lowest frequency for each version between 13 – 5mm for  $max_d = 15m$ , and between 42 – 19cm for  $max_d = 500$ . The frequency per layers with  $max_d = 15m$  are:

- For 64 channels (32 Frequencies) [mm]: 15000.0, 11641.294, 9034.65, 7011.669, 5441.66, 4223.198, 3277.5664, 2543.6743, 1974.111, 1532.0806, 1189.0267, 922.7875, 716.1628, 555.8041, 431.352, 334.7664, 259.8076, 201.6332, 156.4847, 121.4456, 94.2523, 73.1479, 56.7691, 44.0577, 34.1926, 26.5364, 20.5945, 15.9831, 12.4043, 9.6268, 7.4712, 5.7983.
- For 32 channels (16 Frequencies) [mm]: 15000.0, 9034.65, 5441.66, 3277.5664, 1974.111, 1189.0267, 716.1628, 431.352, 259.8076, 156.4847, 94.2523, 56.7691, 34.1926, 20.5945, 12.4043, 7.4712.
- For 16 channels (8 Frequencies) [mm]: 15000.0, 5441.66, 1974.111, 716.1628, 259.8076, 94.2523, 34.1926, 12.4043.

The frequency per layers with  $max_d = 500m$  are:

- For 64 channels (32 Frequencies) [m]: 500.0, 388.0432, 301.155, 233.7223, 181.3887, 140.7733, 109.2522, 84.7891, 65.8037, 51.0694, 39.6342, 30.7596, 23.8721, 18.5268, 14.3784, 11.1589, 8.6603, 6.7211, 5.2162, 4.0482, 3.1417, 2.4383, 1.8923, 1.4686, 1.1398, 0.8845, 0.6865, 0.5328, 0.4135, 0.3209, 0.249, 0.1933,
- For 32 channels (16 Frequencies) [m]: 500.0, 301.155, 181.3887, 109.2522, 65.8037, 39.6342, 23.8721, 14.3784, 8.6603, 5.2162, 3.1417, 1.8923, 1.1398, 0.6865, 0.4135, 0.249.
- For 16 channels (8 Frequencies) [m]: 500.0, 181.3887, 65.8037, 23.8721, 8.6603, 3.1417, 1.1398, 0.4135.

### A.3. Random Depth

We randomize our input depth with  $\frac{1}{4}$  random depth jittered,  $\frac{1}{4}$  rescales between two randomly selected and sorted bins, and  $\frac{1}{4}$  random offsets. The remaining  $\frac{1}{4}$  remains at the original metric depth. The jitter reduces or increases the original depth samples by  $\pm 20\%$ . The offsets are drawn uniformly per depth sample  $d$  from its  $\pm STD(d)$ . The bins are randomly drawn from  $0 - 1m$ ,  $0.5 - 2m$ ,  $0.5 - 5m$ ,  $1 - 15m$ ,  $5 - max_d$  and jittered as well. The depth samples exceeding the maximum training depth  $max_d$  are rescaled to  $max_d \times (0.9 + r0.1)$ , where  $r$  is some uniformly drawn random scalar. This corresponds to a training distribution of  $\approx 21.59 \pm 5.82$  for  $max_d = 500m$ , and a training distribution of  $\approx 2.84 \pm .79$  for  $max_d = 15m$ .

**Random Density** During training, the noise distribution regulates whether the model has handled more depth reconstruction (low threshold) or prediction (high threshold). Rather than having this distribution fixed and balanced in the middle at the training, we shift the distribution from a reconstruction-favoring setting towards a balanced state (see Fig. 4). Thereby, the model can focus on learning to encode-decode depth, before it is more and more challenged to predict missing depth values, which stabilizes our training and gives better results in our experiments. In Fig. 5 we visualize some random Perlin noise

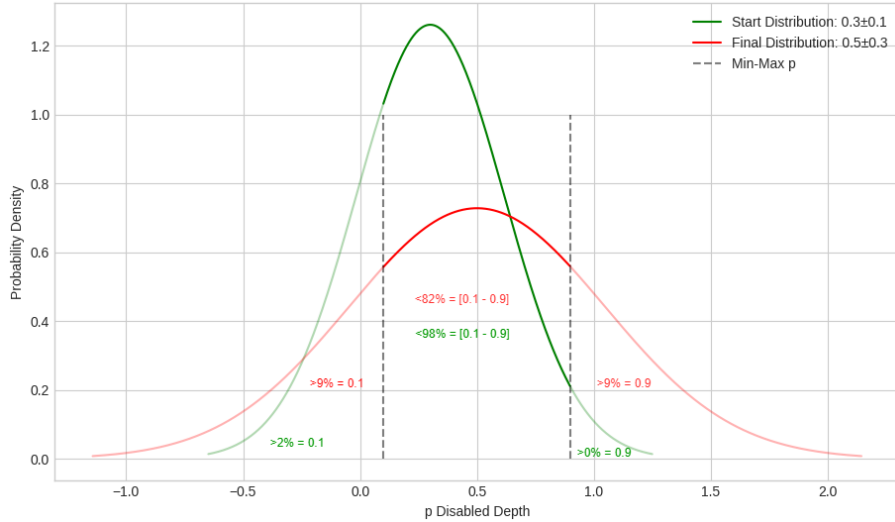


**Figure 4. Noise-Shift:** The threshold distribution for uniform and perlin noise is shifted from "easy" to "hard" instead of being constant. During the warm-up period, the distribution is set to an "easy" setup to prioritize depth reconstruction learning. Subsequently, the distribution gradually shifts to a "harder" setup that demands both depth reconstruction and prediction skills.

generations, and demonstrate how we use them to generate binary masks for our vanishing depth training pipeline (see Sec. 3). Unlike grids or Gaussian noise, Perlin noise does generate rounded shapes in various forms. Thus, we can diversify the noise and mimic the behavior of time of light depth sensors (loss of information) more closely. This in turn allows the depth feature extraction to learn to deal with these fluctuations in the input density.

### A.4. Depth Completion

We use our Decoder trained by our VD pretraining to compare the precision of our methods. We test on the commonly used Kitti (Geiger et al., 2012) and Void (Wong et al., 2020) datasets. Both sets have not been seen by during VD training. Kitti's maximum distance of 80m does exceed our 15m PDE. Therefore, we downscale the depth input to 15m with a sample wise scalar. The prediction is then rescaled with that scalar to fit the original depth distribution. Thus, our PDE can process any depth. However, with increasing the selected frequencies become larger as well. We summarize our results in Table 2 of our paper, in which we reach SOTA results on Void.

### A.5. Classification

We follow DINOv2 and train multiple fully connected classification layers with individual hyperparameters simultaneously on top of our frozen encoders. We use dropouts of  $[0.0:0.1:0.5]$  to embrace RGBD based classification. In combination with

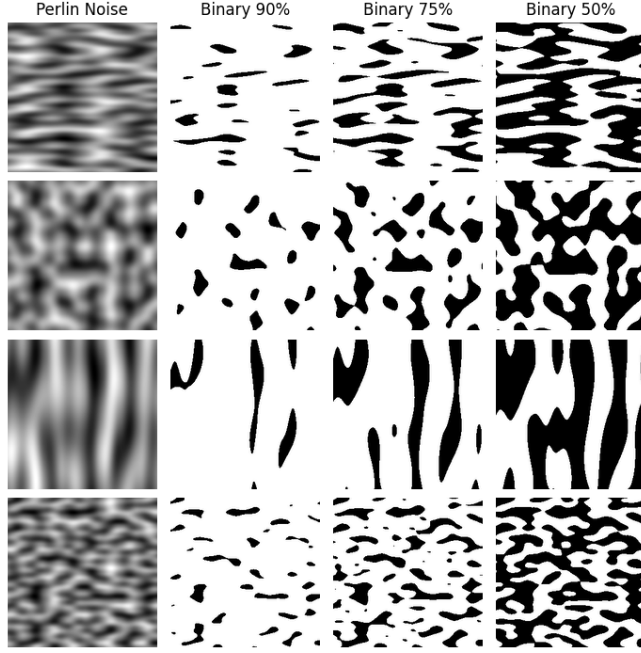


**Figure 5. Perlin noise:** For the in-painting masks, we generate Perlin Noise and convert them to binary masks given some target distribution. Thereby, we are able to remove rounded areas (organic shapes) from the input signal. Our experiments show that this in turn helps the model to reach better results.

the learning rates (lr) [1e-5, 2e-5, 5e-5, 1e-4, 2e-4, 5e-4, 1e-3, 2e-3, 5e-3, 1e-2, 2e-2, 5e-2, 0.1, 0.2] from DINOv2, we train a total of 84 classifiers simultaneously with a resolution of 224. For ImageNet (Deng et al., 2009) (1000 classes) we follow again DinoV2 with a batch size of 1024 and 12.5k training steps, while we reduce to a batch size of 128 and 1k training steps for our smaller problems of NYUv2 (Silberman et al., 2012) (10 scenes), SUN-RGBD (Song et al., 2015) (19 scenes) and MVIP (Koch et al., 2023) (308 Classes). For data augmentation we employ random crops, color jitters, horizontal flips, grayscale, solarization, and gaussian blurring. We report the best of the 84 classifiers in Table 3 of our main paper

## A.6. Segmentation

Using MM Segmentation (Contributors, 2020)<sup>1</sup> we train a commonly used mask2former (Cheng et al., 2022) segmentation head on top of our frozen encoders. We select mask2former as it is a general method working well for any encoder or datasets. We use a resolution of 518 for our Vit/14 (patch-size) and 512 for Omnivore/16 with a batch size of 16, and train for 20k steps on NYUv2 (Silberman et al., 2012) and SUN-RGBD (Song et al., 2015), and 30k steps on the larger ADE20k (Zhou et al., 2017) and COCO-Stuff (Caesar et al., 2016) datasets. We again use ViT fusion layers [3, 6, 9, 12] for the gradual decoding following (Ranftl et al., 2021; Oquab et al., 2023). For data augmentation, we employ again random crops, color jitters, flips, grayscale, solarization, and Gaussian blurring. During validation, we are using the original resolution of the individual samples. We summarize our segmentation results in Table 4 of your main paper, where we obtain the SOTA results of 56.05 mIoU on SUN-RGBD.

## A.7. 6D Object Pose Estimation

We train a PoET (Jantos et al., 2022) 6D object pose estimation head on top of our frozen encoder weights with a batch size of 48 for 90k steps and only color augmentations. We use PoET as it follows the general decoding method of Deformable DETR (Zhu et al., 2021), can be added on top of any encoder, and requires no post-processing or (often iterative) second stage. Following PoET we use a lr of 2e-4 for the decoder head, while the linear project layers are trained with a lr of 1e-5. We train our pose estimation models for YCV-Video (Xiang et al., 2017) (including the 80k synthetic training samples), Homebrew (Kaskman et al., 2019), and LM-O (Brachmann et al., 2014), which are from the commonly used BOP (pose

<sup>1</sup><https://github.com/open-mmlab/mmsegmentation>, state of January 28th 2025

estimation) challenge (Hodan et al., 2024). YCB-Video features 21 objects with less than 10 objects per scene. The Sim2real challenge of HomeBrew has 33 objects, sometimes more than 20 objects per scene. Therefore, we extend PoET’s default number of 10 decoding queries to 30. LM-O has 8 objects with the challenge of relative high occlusion. For these downstream tasks, we also investigate our P3DE encoder, which is trained to encode 3D point clouds (see Sec. 3.1 for more details). For our pose estimation results see. Tab 5 in our main paper.

### A.8. Omnivore Implementation

For Omnivore we use the official pipeline and implementation<sup>2</sup>. For their disparity map generation we use their implementation shared on github<sup>3</sup>:

```

import numpy as np
import torch
from PIL import Image

sensor_to_params = {
    "kv1": {
        "baseline": 0.075,
    },
    "kv1_b": {
        "baseline": 0.075,
    },
    "kv2": {
        "baseline": 0.075,
    },
    "realsense": {
        "baseline": 0.095,
    },
    "xtion": {
        "baseline": 0.095, # guessed based on length of 18cm for ASUS xtion v1
    },
}

def convert_depth_to_disparity(depth_file, intrinsics_file, sensor_type, min_depth=0.01, max_
    """
    depth_file is a png file that contains the scene depth
    intrinsics_file is a txt file supplied in SUNRGBD with sensor information
        Can be found at the path: os.path.join(root_dir, room_name, "intrinsics.txt")
    """
    with open(intrinsics_file, 'r') as fh:
        lines = fh.readlines()
        focal_length = float(lines[0].strip().split()[0])
        baseline = sensor_to_params[sensor_type]["baseline"]
        depth_image = np.array(Image.open(depth_file))
        depth = np.array(depth_image).astype(np.float32)
        depth_in_meters = depth / 1000.
        if min_depth is not None:
            depth_in_meters = depth_in_meters.clip(min=min_depth, max=max_depth)
        disparity = baseline * focal_length / depth_in_meters
        return torch.from_numpy(disparity).float()

```

<sup>2</sup><https://github.com/facebookresearch/omnivore>, state of the 28th of January 2025

<sup>3</sup><https://github.com/facebookresearch/omnivore/issues/12>, state of the 28th of January 2025

For the further data pipeline we use again the official implementation<sup>4</sup> of:

```

# convert depth [mm] to disparity
disparity = convert_depth_to_disparity(depth)
rgbd_transform = T.Compose(
[
    DepthNorm(max_depth=75.0, clamp_max_before_scale=True),
    T.Resize(224),
    T.CenterCrop(224),
    T.Normalize(
        mean=[0.485, 0.456, 0.406, 0.0418],
        std=[0.229, 0.224, 0.225, 0.0295]
    ),
]
)
image = T.ToTensor()(image)
depth = disparity[None, ...]
rgbd = torch.cat([image, depth], dim=0)
rgbd = rgbd_transform(rgbd)

# The model expects inputs of shape: B x C x T x H x W
rgbd_input = rgbd[None, :, None, ...]
prediction = model(rgbd_input.to(device), input_type="rgbd")

```

We used the focal length and camera baseline on SUN-RGBD as described above. We derive the focal length by  $\min(\text{height}, \text{width})^5$  and set the camera baseline to 0.05<sup>6</sup> when the downstream task dataset does not give the focal length and camera baseline, respectively. For 6D object pose estimation and our VD training for depth completion, we keep the focal length and camera baseline constant. This preserves the metric depth information in disparity maps, which allows encoder to infer metric depth distances. For your experiments, we load the Omnivore Swin B weights pretrained on ImageNet21k.

#### A.9. EVA02

For EVA02 we use the official implementation and models<sup>7</sup>. For your experiments, we load the EVA02 Vit-B weights MIM-pretrained on ImageNet21k<sup>8</sup>.

#### A.10. DinoV2

For DinoV2 we use the official implementation and models<sup>9</sup>. For your experiments, we load the DinoV2 Vit-B distilled weights without registers.

## B. Studies on Positional Depth Encoding (PDE) and Model Stability

In Fig. 6 we show the effect of chaning the input density for PDE and Norm-based depth encoding. In Fig. 7 and Fig. 8 we investigate the effect of changing the input distribution w.r.t. depth completion precision. In Table 7 we analyze the effect of changing the input distribution w.r.t. segmentation performance on SUN-RGBD (Song et al., 2015). Here we see that Omnivore (Girdhar et al., 2022) suffers from a changing depth distribution, which is not as much the case for our VD

<sup>4</sup>[https://colab.research.google.com/github/facebookresearch/omnivore/blob/main/inference\\_tutorial.ipynb](https://colab.research.google.com/github/facebookresearch/omnivore/blob/main/inference_tutorial.ipynb), state of the 28th of January 2025

<sup>5</sup>A general approximation as the focal length is relative to the resolution.

<sup>6</sup>Baseline of the commonly used Realsense RGBD Camera D435: <https://www.framos.com/en/products/depth-camera-d435-camera-only-20802>, state of the 28th of January 2025

<sup>7</sup><https://github.com/baaivision/EVA/tree/master/EVA-02>, state of the 28th of January 2025

<sup>8</sup><https://github.com/baaivision/EVA/tree/master/EVA-02/asuka>, state of the 28th of January 2025

<sup>9</sup><https://github.com/facebookresearch/dinov2>, state of the 28th of January 2025

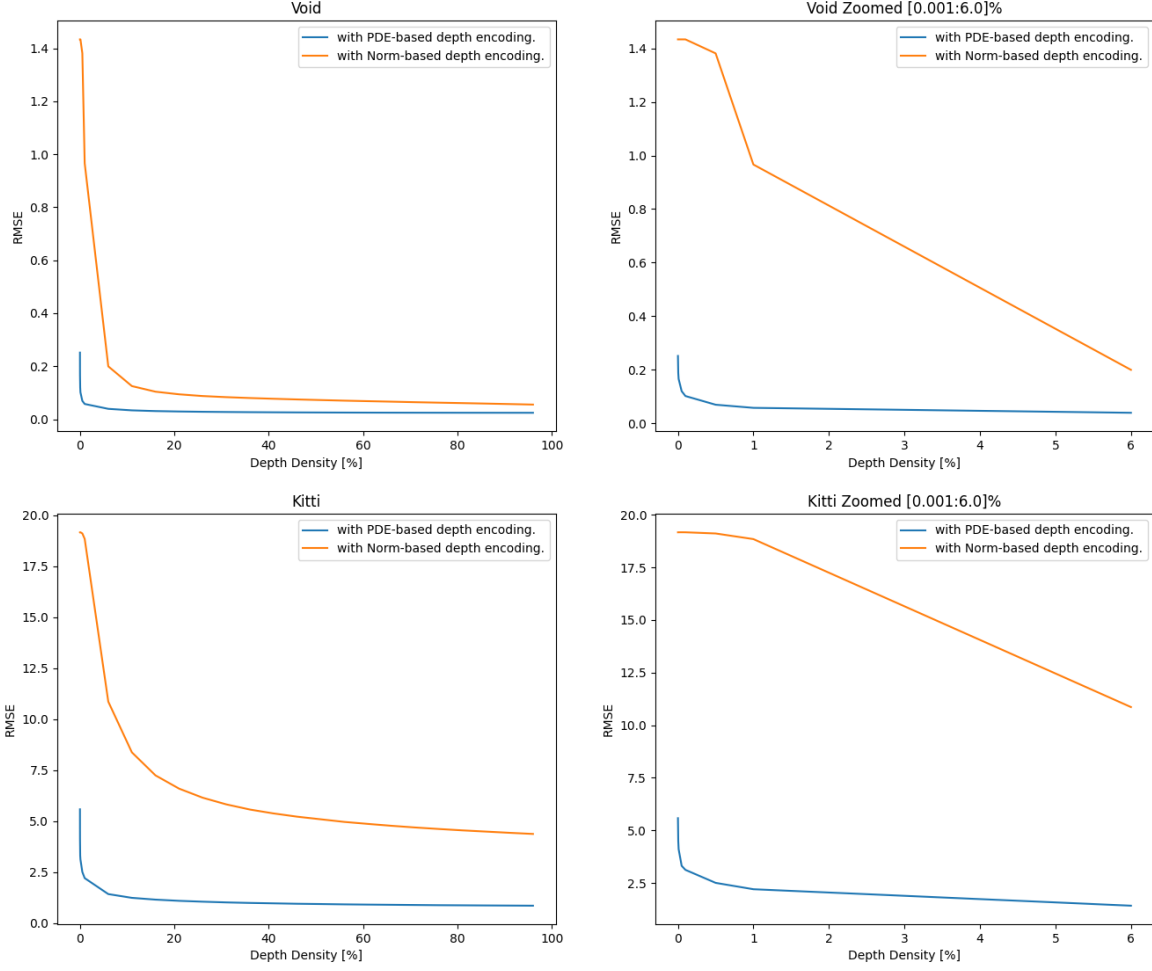


**Figure 6. Effects of Increasing Depth Input Density:** From the graphs one can see that PDE is very suited to encode very sparse depth input. This is not the case for the Norm-based depth encoding, which suffers very much from densities below 1%. PDE is capable to complete depth with almost its full precision with only a few % of the depth distribution. This enables further application such as denoising corrupted input or to upsample precise but sparse lidar (laser) depth measurements.

encoders. Additionally, in Tab. 8 we analyze for each encoding method how much depth and RGB information are fused within each encoder stage. Here, one can explore some trends w.r.t. the amount of depth and RGB embeddings within the depth encoder.

### C. Multi-Scale Balanced Scale-Invariant Loss

Within this section, we outline our "Multi-Scale Balanced Scale-Invariant Loss". The loss function is build upon the pixel wise Scale-Invariant (SI-Loss) loss (Eigen et al., 2014) implementation by Adabins (Bhat et al., 2020):

$$\mathcal{L}_{SI} = \alpha \sqrt{\frac{1}{T} \sum_i g_i^2 - \frac{\lambda}{T^2} (\sum_i g_i)^2} \quad (3)$$

where  $g_i = \log \hat{d}_i - \log d_i$ ,  $\hat{d}_i$  is the depth prediction at pixel index  $i$  and  $d_i$  its ground truth (pixels without depth ground truth are ignored). The constants  $\lambda = 0.85$  and  $\alpha = 10$  are used to balance the two loss terms (Bhat et al., 2020). Given our vanishing depth mask  $\mathcal{M}$  (the removed input depth pixels), we use the SI-loss twice; first (1) on pixel wise depth

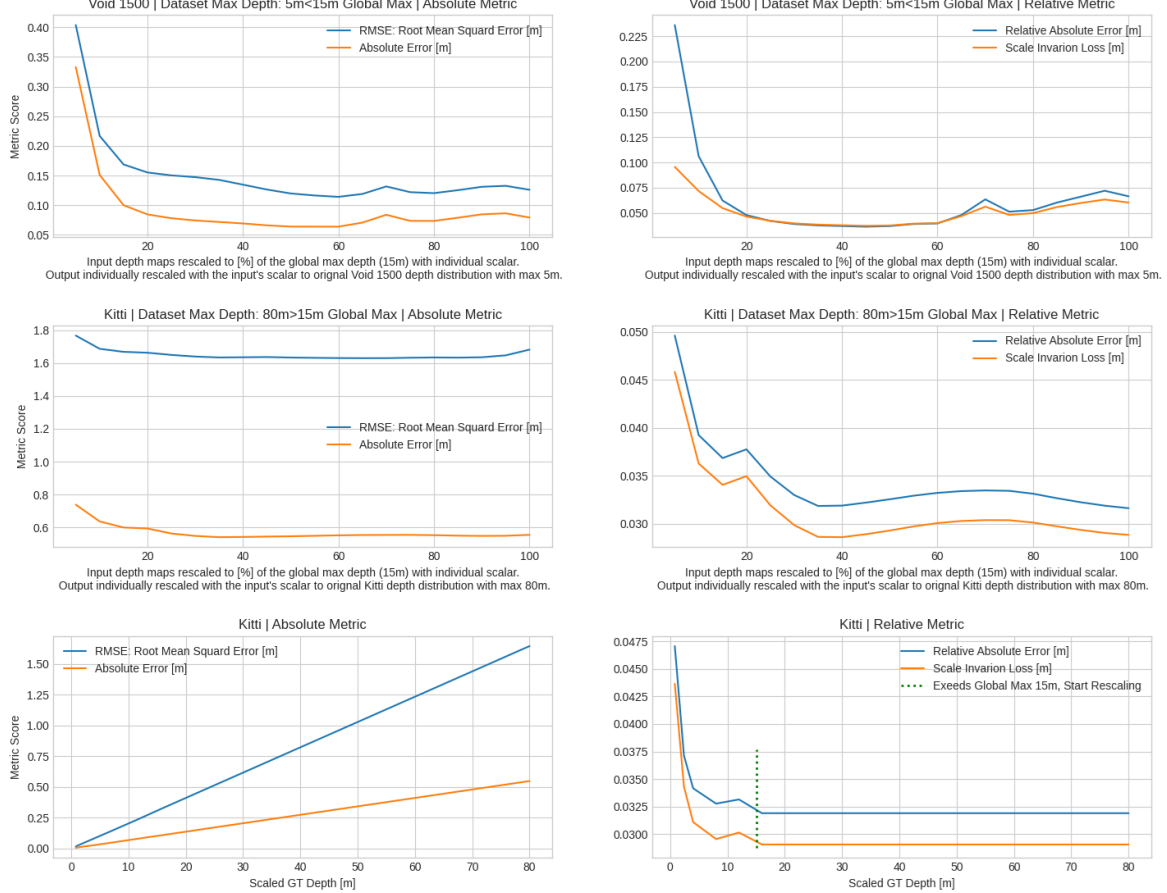


**Figure 7. Effects of Compressing and Increasing Depth PDE-based Encoding:** These effects are measured for DinoV2+VD(PDE) (see Sec. 5 in our main paper). In the first and second row we show the absolute and relative depth completion results when compressing (if applicable stretching for Void) the original depth input into a proportion [%] of the max depth (15m). Note, that we rescale the output with the respective scalar used for the compression. Hence, every point is predicting the same target distribution. Here we observe that PDE is working best and relative stable when using at least 20-30% of its encoding range with a sweet spot at 40%. In the bottom row we scale the ground truth for Kitti. Thus the target distribution is increasing. Here we observe the same phenomena when compressing when not using the full span of PDE. When exceeding the point of compression, one can observe that the absolute errors are increasing linear and the relative errors are stable.

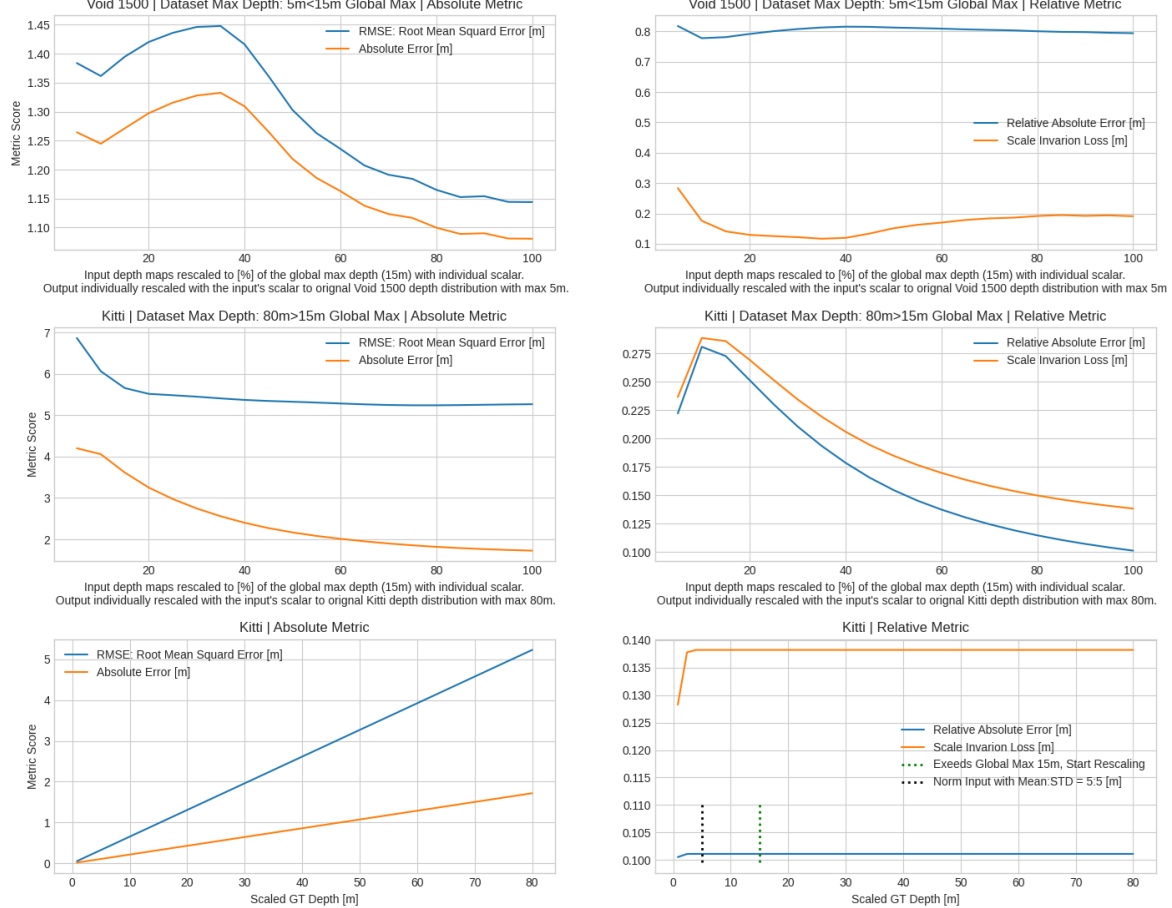


**Figure 8. Effects of Compressing and Increasing Depth Norm-based Encoding:** These effects are measured for DinoV2+VD(Norm) (see Sec. 5 in our main paper). In the first and second row we show the absolute and relative depth completion results when compressing (if applicable stretching for Void) the original depth input into a proportion [%] of the max depth (15m). Note, that we rescale the output with the respective scalar used for the compression. Hence, every point is predicting the same target distribution. Here we observe that Norm-based depth encoding yield unstable outputs when getting changing depth distributions without clear trends. In comparison to PDE, one can see that the precision in depth completion is unstable, less predictable, and without a clear sweet spot. In the bottom row we scale the ground truth for Kitti. Thus the target distribution is increasing. When exceeding a certain threshold distribution, one can observe that the absolute errors are increasing linear and the relative errors are stable, just like the PDE-based depth encoding. However, it has a higher baseline.

**Table 7. Scale & Density Invariance Results:** We train again a mask2former (Cheng et al., 2022) on the frozen method-based pretrained RGBD-encoders. We compare the ability of the different encoders to cope with change depth distributions and densities. \* Most depth maps are rescaled to the depth limit of 15m, since we rescale everything where the max limit is exceeded.

Task→		Semantic Segmentation								
Dataset & Metric→		Sun-RGBD mIoU (Abs. SOTA 54.6 (Jia et al., 2024))								
Random Zeros[%]→	100	99.9	99	50	0	0	0	0	0	
Depth Scale→	0	1	1	1	1	0.1	0.5	2	5*	
Depth Mean →	0	4.6	4.6	4.6	4.6	.46	2.3	6.5	7.1	↓
Depth STD →	0	1.5	1.5	1.5	1.5	.15	.79	2.1	2.2	vs.
Depth Zeros [%] →	100	99.9	99	58	16	16	16	16	16	RGB Only
Method↓										
Omnivore		47.06	45.29	45.01	35.25	40.93	43.46	45.02	45.56	45.07
EVA-02 + VD(PDE) [Ours]		42.76	43.69	44.04	43.75	44.06	44.06	44.08	44.29	44.54
DinoV2 + VD(PDE) [Ours]		<b>55.63</b>	<b>55.14</b>	<b>55.64</b>	<b>56.01</b>	<b>56.05</b>	<b>55.22</b>	<b>55.50</b>	<b>55.28</b>	<b>55.19</b>
										<b>53.75</b>

**Table 8. Amplitude of rgb signal in depth encoder:** We use S&E (Hu et al., 2017) RGB-D fusion at their corresponding fusion-layers index 3, 6, 9 & 12. Here, the depth and RGB signals are weighted and fused by an addition before being forwarded to the next depth encoder layer. Here we report the relative amplitude of the RGB signal before fusion. Thereby, we indicate the contribution of the both the RGB and depth signals towards our mean AUC RMSE training results for each model (see Tab. 1). Utilizing our positional depth encoding (PDE) we see an decrease in signal strength in Layer-3 coming from the RGB initial feature extraction. We conclude that the extracted depth features from PDE are more valuable than if a simple normalization based depth encoding method was used. For our experiments without DINOv2 Weights, we see a much lower amount of RGB embeddings in the Depth Encoder. This might indicate a loss in RGB-feature value, which aligns with the superiority of using DINOv2 pretrained weights throughout our experiments. General trends within the methods can be seen and encoding methods can be grouped together within every layer depth. However, these numbers are not telling a clear story.

	Encoder Specifications			VD Training Settings			% of RGB-Embeddings			
	RGBD Encoder		Depth Encoding Method	Frozen Encoder		Max Distance Decoder	Fused into the Depth Encoder			
				RGB	Depth		Block-1 Layer-3	B.-2 L.-6	B.-3 L.-9	B.-4 L.-12
	Encoder	Pre-Trained								
Baselines	2×Vit-B	DinoV2	Norm Disp.	✓	-	15m	90.97	71.19	59.09	77.21
	2×Vit-B	DinoV2	Norm 2.4±.8	✓	-	15m	91.35	73.85	59.32	77.87
	2×Vit-B	DinoV2	Norm 5±5	✓	-	15m	80.81	62.87	61.58	73.02
	2×Vit-B	DinoV2	Norm 21±6	✓	-	500m	90.94	76.31	61.08	66.31
	2×Vit-B	DinoV2	PDE 16C	✓	-	500m	84.02	66.25	60.97	81.74
	2×Vit-B	DinoV2	PDE 32C	✓	-	500m	87.04	66.07	61.25	79.31
	2×Vit-B	DinoV2	PDE 64C	✓	-	500m	88.76	68.81	61.43	80.87
With PDE	2×Vit-B	DinoV2	PDE 32C	✓	-	15m	82.94	61.10	63.18	85.93
	2×Vit-B	DinoV2	PDE 64C	✓	-	15m	84.73	63.07	63.93	84.95
	2×Vit-B	DinoV2	PDE 32C-fix	✓	-	15m	83.32	63.56	62.41	82.58
	2×Vit-B	DinoV2	PDE 64C-fix	✓	-	15m	86.12	68.48	61.57	83.37
	2×Vit-B	EVA-02	PDE 32C-fix	✓	-	15m	60.78	69.25	72.64	83.58
	2×Vit-B	-	PDE 32C-fix	-	-	15m	56.67	69.80	65.68	65.34

reconstruction ( $i \notin \mathcal{M}$ ), and afterwards (2) on pixel wise depth estimation ( $i \in \mathcal{M}$ ):

$$\mathcal{L}_{pixel} = \begin{cases} \mathcal{L}_{SI}(1) & , \text{if } i \notin \mathcal{M} \\ \mathcal{L}_{SI}(2) & , \text{if } i \in \mathcal{M} \end{cases} \quad (4)$$

The final "multi-scale" (MS) part of our loss is simply computing  $\mathcal{L}_{pixel}$  at multiple output resolutions (see Sec. 3):

$$\mathcal{L}_{MS} = \sum_{\mathcal{F}} \mathcal{L}_{pixel}(\mathcal{R}(\mathcal{M}, \hat{d}, d, \mathcal{F})) \quad (5)$$

where  $\mathcal{R}$  is a resize function given some resize factor  $\mathcal{F}$ . Here, we use equal (no) weighing of the multi-scale losses, which leaves every output equally important.

## D. Visual Qualitative Results

In the remainder of our supplementary material, we visualize some qualitative results of our depth encodings, depth completion, and depth estimation. In Fig. 9 we show a further extension of our depth encoder embeddings from Fig. 3. Additionally, we visualize the depth encoder embeddings on the RGB-Only input from ADE20k (Zhou et al., 2017) (see Fig. 10). Eventually, we compare some completed point clouds with the original in Fig. 11 and 12.

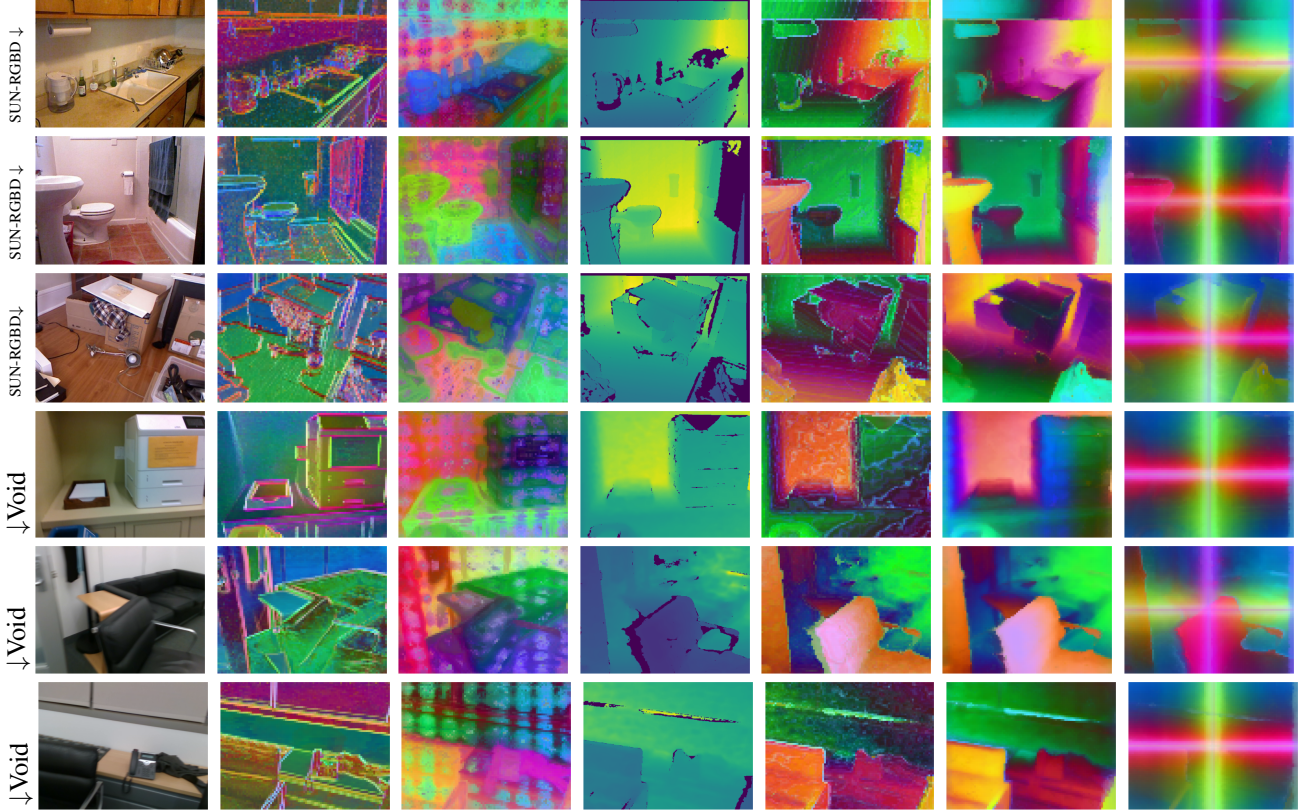


**Figure 9. Visualization of Embeddings (extension of Fig. 3):** Following DINOv2 we use PCA to reduce embedded attention maps to three channels (RGB), which are visualized above in the columns (b, c, e, f & g). The columns (b & c) are the corresponding color embeddings of (a). The columns (e, f, & g) are the corresponding depth embeddings of (d). (b) and (e) are trained from scratch, while for (f & g) we start training with DINOv2 weights (Oquab et al., 2023). Here, the DINOv2 RGB encoder (c) stays frozen during our VD training. The DINOv2 RGB encoder (c) shows good semantic understanding, while our RGB encoder trained from scratch (b) is showing edge detection with some hint of semantic understanding. Our depth encoders (e & f) show specialization on depth awareness, but (f) clearly benefits from the DINOv2 weights. Our model trained on 3D point clouds (g) (see section 3.1 & A.7) shows perception of the encoded XYZ axis.

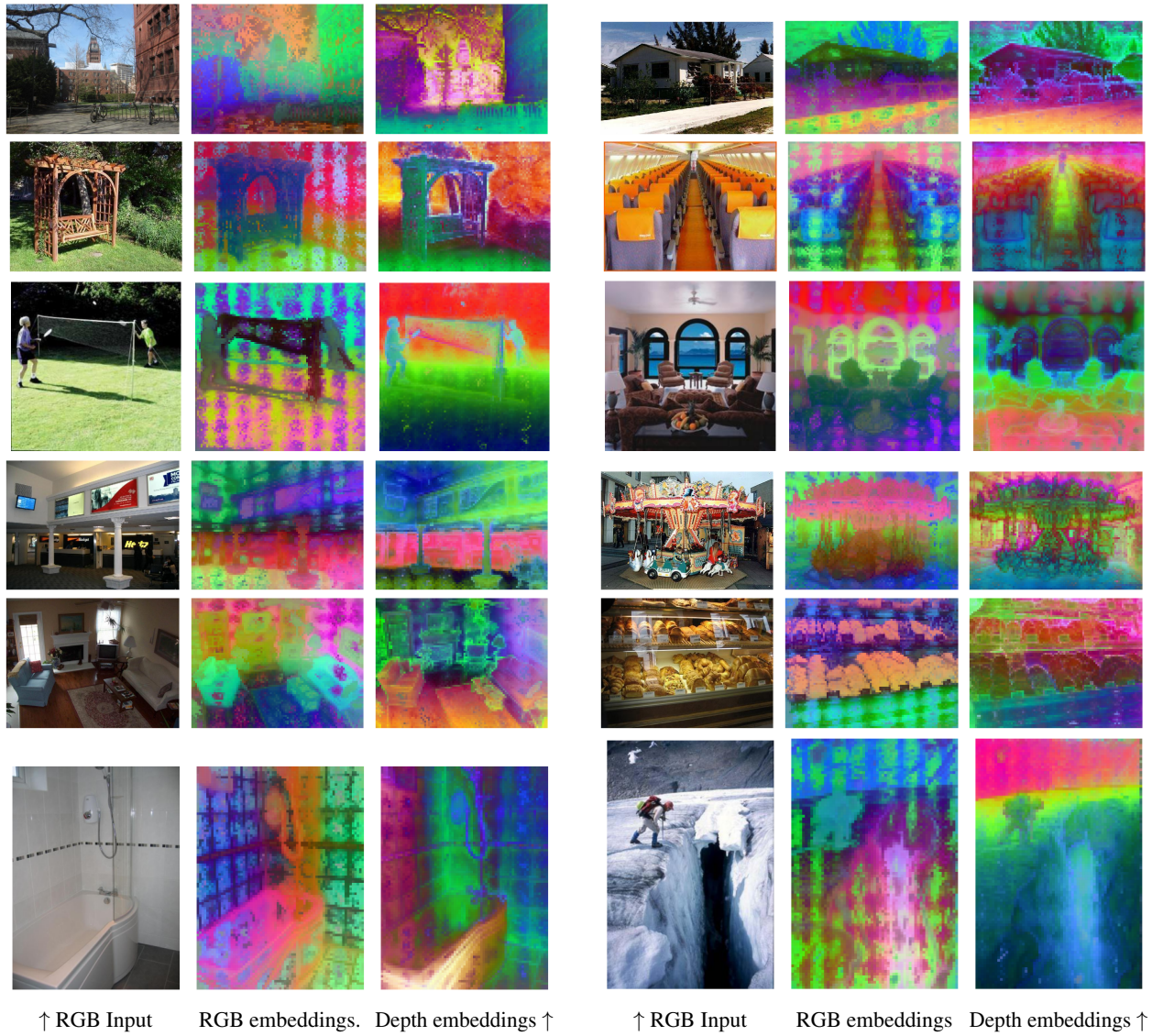


**Figure 10. Visualization of Embeddings Without Depth Image:** We observe the attention maps above given only the RGB image and a zero initialisation of the depth image(visualized to RGB via PCA). One can see that the depth embeddings are showing depth awareness. (All images are taken from the ADE20K (Zhou et al., 2017) segmentation validation split. The ADE20K dataset is not part of our training pipeline, see table. 6).



**Figure 11. Colored point cloud visualization (two views) (SUN RGB-D (Song et al., 2015)):** On the top, two views are shown of the original point cloud, while on the bottom, we show a completed version from similar view points. One can observe that our model completed the depth image such that the resulting 3D point cloud is now filling holes, which were previously empty.

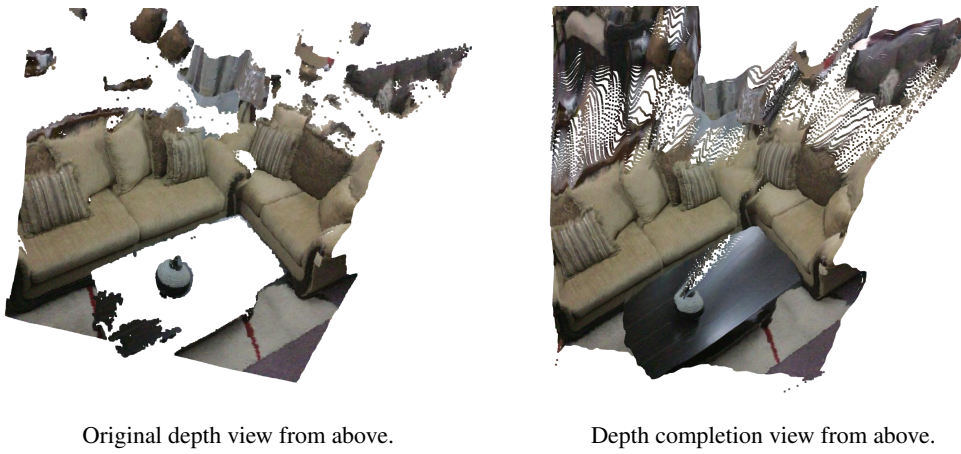


**Figure 12. Colored point cloud visualization (from above) (SUN RGB-D (Song et al., 2015)):** On the left the original point cloud is shown, while on the right we show a completed version from a similar view points. Here we can show that our model completes the desk, which were previously mostly incomplete. The area behind the vase not visible, hence it remains incomplete. Moreover, one has to notice that our model stretches depth prediction values between large depth gabs, which should have stayed as gabs.